Remote Sensing Information for Urban Planning of Barisal Town and Surrounding

Hannover, September 2021

BGR Bundesanstalt für Geowissenschaften und Rohstoffe

german cooperation
DEUTSCHE ZUSAMMENARBEIT

Authors:	Lukas Wimmer (BGR), Chapter 2.1-2.3 Nicolas Wagener (BGR), Chapter 1

Commissioned by:	Federal Ministry for Economic Cooperation and Development (Bundesministerium für wirtschaftliche Zusammenarbeit und Entwicklung, BMZ)
Project:	Geo-Information for Urban Planning and Adaptation to Climate Change (GPAC)
Project Number:	2016.2062.4
BGR Number:	05-2394
ELVIS Number:	B80136-01_06 05-2394 TZ Bangladesch-III
Project Partner:	Geological Survey of Bangladesh (GSB)

Pages:	71
Place and date of issuance:	Hannover, 08. September 2021

To be cited as:

Wimmer, L. and Wagener, N. (2021): Remote Sensing Information for Urban Planning of Barisal Town and Surrounding, BGR Project Number: 05-2394.

Summary

Authors: Lukas Wimmer, Nicolas Wagener

Title: *Remote Sensing Information for Urban Planning of Barisal Town and Surrounding*

Keywords: Land-Use Classification; River Change Detection; Inundation Mapping

The products of this report aim to provide support for urban planning for the city of Barisal and its surrounding areas. Based on optical and radar satellite data, maps on recent land use and urban development, river course changes and rainy season inundation are created.

A dense urban centre running along the Kirtonkhola River characterizes land-use in the city of Barisal. The suburbs are dominated by rural settlements that lie in close proximity to agricultural used land. Frequent inundation is visible in the riverine areas and in areas that belonged to a river in the past. The city centre does not experience seasonal inundation. Significant anthropogenic overprints of former riverbeds by agricultural land-use and settlement development are identified using the river shifting change detection in the surroundings east of Barisal.

Table of Contents

List of Figures

Annexure A

List of Tables

List of Abbreviations

ASF	Alaska Satellite Facility
BBD	Bodenbewegungsdienst Deutschland (German Ground Motion Service)
BGR	Bundesanstalt für Geowissenschaften und Rohstoffe (Federal Institute for Geosciences and Natural Resources)
BWDB	Bangladesh Water Development Board
dB	Decibel (unit)
DEM	Digital Elevation Model
DOS	Dark Object Subtraction
ESA	European Space Agency
GNSS	Global Navigation Satellite System
GPAC	Geo-Information for Urban Planning and Adaptation to Climate Change
GPS	Global Positioning System
GSB	Geological Survey of Bangladesh
InSAR	Interferometric Synthetic Aperture Radar
Landsat MSS	Landsat Multispectral Scanner System
Landsat OLI	Landsat Operational Land Imager
Landsat TM	Landsat Thematic Mapper
LEDAPS	Landsat Ecosystem Disturbance Adaptive Processing System
NASA	National Aeronautics and Space Administration
NIR	Near Infrared
NDWI	Normalized Difference Water Index
PSI	Persistent Scatterer Interferometry
RADAR	Radio Detection and Ranging
SAR	Synthetic Aperture Radar
SBAS	Small Baseline Subset
SRTM	Shuttle Radar Topography Mission
SWIR	Shortwave Infrared
TIR	Thermal Infrared
UAV	Unmanned aerial vehicle
USGS	United States Geological Survey

1 Introduction to Remote Sensing

Remote sensing has been variously defined, but basically is the science that describes the collection of physical information, interpretation and extraction of information acquired over an object or area of interest without having physical contact, by the use of remote sensing instruments. The term information refers to a wide range of observable quantities, such as reflected solar radiation across the electromagnetic spectrum and emitted thermal radiation measured from handheld, unmanned aerial vehicle (UAV), airborne or spaceborne imaging sensors and received back-scattered microwave radiation equipment. Availability and effective exploitation of such data has facilitated advances in many applied fields (CHAMBELL, 1996; USTIN, 2004)

The availability and capacity of remote sensing data is comprehensive and huge, therefore the application of remote sensing data to identify and monitor land surfaces and environmental conditions has expanded enormously and remotely sensed data are an essential tool in natural resource management. Climatic changes, desertification processes, forest fires, glaciers melting, water pollution, land cover and vegetation status can be observed thanks to remote sensors onboard of aircraft or satellites orbiting around the earth. Remote sensors onboard of aircraft and satellites allow for a synoptic view of the earth surface at different wavelengths of the electromagnetic radiation at the same time (multi-spectral, -frequency), with (high-) frequent time interval and scale (multi-resolution).

Sensors can be divided into two groups: Passive sensors depend on an external source of energy, usually the sun. Sun radiation is reflected and emitted from the earth surface and collected by a wide variety of optical sensors. Active sensors have their own source of energy. These sensors send out a signal and measure the amount reflected back, and do not depend upon varying illumination conditions (PRASAD ET AL., 2011) (see Fig. 1).

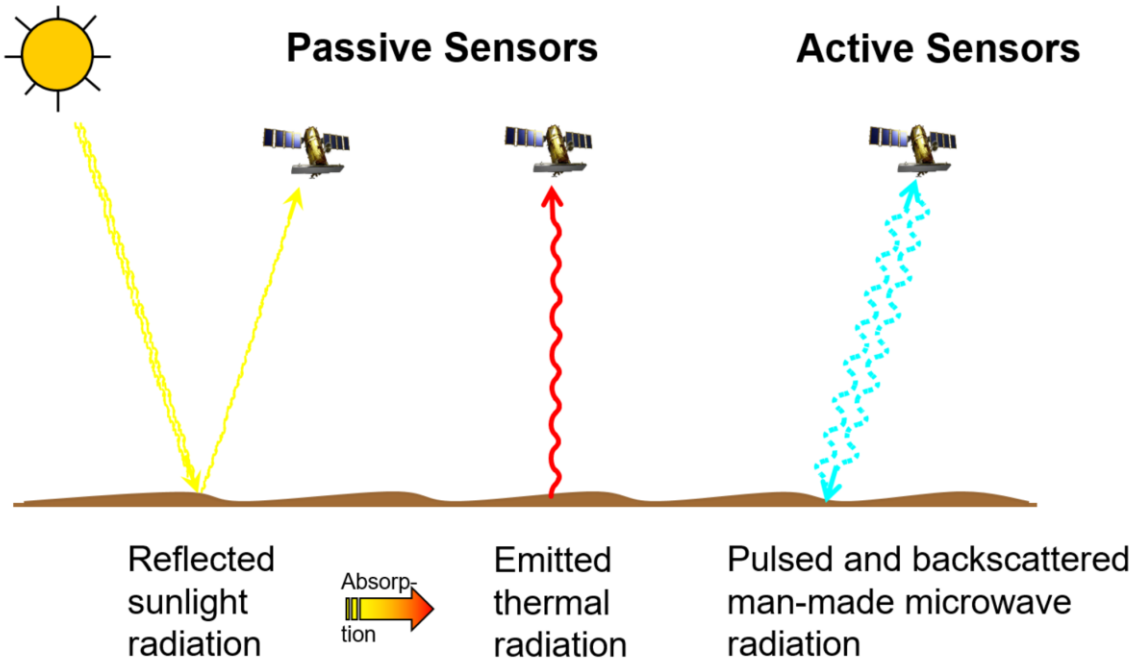

Figure 1: *Passive and active sensors (Source: BGR).*

1.1 Fundamentals of Optical Remote Sensing

Optical remote sensing involves acquisition and analysis of optical data, based on solar illumination and the detection of electromagnetic radiation reflected from targets on the ground. Optical Remote Sensing deals with those part of electromagnetic spectrum characterized by the wavelengths from the visible (from 0.4 µm) to the near infrared (NIR) and short wave infrared (SWIR) up to thermal infrared (TIR, 15 µm), collecting radiation reflected and emitted from the observed surfaces (see Fig. 1).

Optical remote sensing is a passive technique for earth observation, which is exposed to a strong interaction of the electromagnetic radiation within the atmosphere at its operating frequencies and to the presence of clouds. Both factors constitute important limitations on the potential observation of the earth's surface.

Analysis is based on the spectral differences of materials, as materials reflect and absorb differently at different wavelengths, resulting in a specific and unique "spectral footprint". Thus, the targets can be differentiated by their spectral reflectance signatures in the remotely sensed images (SABINS, 1996; RENCZ, 1999).

Optical remote sensing systems are classified depending mainly on the number of spectral bands used in the imaging process. Advances in imaging hardware enabled availability of high spatial, spectral and temporal resolution (PRASAD ET AL., 2011).

A wide range of applications is still based on multispectral imaging systems e.g. Sentinel-2, Landsat-OLI, even so hyperspectral sensors show rapid development on all platforms from UAV to spaceborne carriers.

1.2 Fundamentals of RADAR Remote Sensing

RADAR is an acronym for *RA*dio *D*etection *A*nd *R*anging and describes an object-detection and active imaging system using radio waves (see Fig. 1). The electromagnetic waves used for imaging radars have wavelengths in the order of several centimeters up to roughly one meter. Since earth's atmosphere has a high penetrability in this part of the electromagnetic spectrum, radar-imaging systems are highly independent from weather conditions in the atmosphere.

The accuracy of an imaging radar is defined by two measures: the resolution along the line-of-sight (range resolution) and the resolution along the flight path of the carrier platform (azimuth resolution). The azimuth resolution depends on the antenna aperture: the larger the distance to the area of interest, the larger the antenna must be. For space-borne missions this leads to unrealistic demands on the size of the antenna mounted on the satellite (WOODHOUSE, 2006). To overcome this obstacle, Synthetic Aperture Radar (SAR) exploits the Doppler Effect to synthesize a larger virtual antenna through the combination of several return signals (echoes).

The signal received at the sensor has a frequency variation induced as a result of the platform motion. This effect is known as Doppler shift, a well-known phenomenon in physics. Since the resolution depends on the time, a particular object on the ground is illuminated by the radar beam, making use of the Doppler shift to combine several backscattered echoes effectively results in increasing the duration of irradiation. As this is in effect equal to increasing the antenna aperture size of which the illumination time is a direct function, the term Synthetic Aperture Radar (SAR) is used to describe such an imaging system (RICHARDS, 2009).

SAR sensors are usually mounted on an airborne or space-borne platform and have a side-looking imaging geometry. While the carrier platform moves forward, the SAR system continuously emits and receives electromagnetic pulses. The emitted radiation interacts with objects on the surface that will then backscatter a portion of the signal to the sensor. How big that portion will be, depends on the physical and electrical properties of the objects (FORNANO & PASCAZIO, 2014). At the sensor, both amplitude and phase of the backscattered signal are received (MOREIRA ET AL., 2013).

While the amplitude is related to the object properties (material, roughness, dielectric properties, etc.), the phase is a function of the sensor-target distance.

Synthetic aperture radar (SAR) remote sensing is used today in a wide range of applications and offers a number of complementary and additional capabilities with regard to optical remote sensing. For instance, it can be used to acquire images at night and almost weather independent, to determine soil moisture, biomass or to measure terrain deformations. The ranging capabilities of SAR are used in various ways. Radar interferometry (InSAR) is one such application and allows the estimation of ground deformation and / or topography from (at least) two SAR acquisitions making use of the phase information contained in both images. Multi-temporal InSAR approaches such as Persistent Scatterer Interferometry (PSI) allow the precise estimation (with millimeter accuracy) of surface deformation for specific point targets over long time periods.

2 Products

2.1 Land-use Map

The fast growing population and the trend to move to urban areas leads to a dynamic change in land use. New urban areas are developed by filling agricultural land with river sand to make the building ground more resilient to flooding (see Fig. 2).

The overall goal of this analysis is the comprehensive mapping of the 2019 land-use in Barisal to derive information on existing and newly established filled areas. The resulting maps will be used in further analyses together with a geomorphological map as a basis for the regionalization of drilling points. Freely available optical satellite data and a supervised classification method allow for the mapping of the land-use.

Figure 2: *Filling of agricultural land with river sand in Faridpur. Photo: L. Wimmer, 11/2019.*

Land-use maps using the classes “Water”, “Bare Soil”, “Urban”, “Rural Settlements” and “Agriculture” are provided for November 2019. An overview map shows the land-use of the study area as well as the surrounding rural areas (Fig. A2). A map, focusing on the study area presents the land-use within the city of Barisal (Fig. A3).

The main focus of this analysis is the distribution of filled and non-filled areas from the land-use map by reclassification of the five above-mentioned classes. A third map presents these areas within the study area of Barisal (Fig. A4).

To process the land-use maps, a supervised classification method based on interactively selected training areas is used. These areas are interactively chosen from the original satellite image and represent the spectral properties of a certain land-use class. The supervised classification classifies the satellite image by comparing all the image values with the selected training areas.

Data

The land use classification is based on a cloud-free image from the Copernicus Sentinel-2 mission for the period of the Bangladesh dry season between October and April and the transition times before and after it. To be able to receive results on the most recent land-use and in order to map water areas comprehensively, a satellite image from the early dry season 2019/2020 is required. Different atmospheric conditions during the sensing times of the images can result in different image features of the same ground objects. Therefore, atmospheric corrected images are mandatory, to allow comparison with future land use maps based on Sentinel-2 data. An atmospheric correction eliminates the atmospheric effects in an image and results in a surface reflectance image that characterizes the spectral surface properties. The atmospherically corrected image, showing the overview area cloud-free, from the 28. November 2019 is used for further processing (see Annexure C: Data).

As input for the land use mapping, all bands with the resolution of 10m and 20m of the image are used (Tab. 1). This selection enables the classification method to accurately characterize the land-use classes by using all available spectral properties of the ground objects.

Table 1: *Overview of the Copernicus Sentinel-2 satellite image used for the classification. Blue color represents the spectral band subset used in the analysis.*

Sensing Date	Bands		Wavelengths	Spatial Resolution
28.11.2019	1	Coastal Aerosol	417nm – 471nm	60m
	2	Blue	399nm – 595nm	10m
	3	Green	515nm – 605 nm	10m
	4	Red	627nm – 703nm	10m
	5	Near Infrared	685nm – 723nm	20m
	6		722nm – 758nm	20m
	7		754nm – 810nm	20m
	8		690nm – 980nm	20m
	8A		832nm – 898nm	20m
	9	Water Vapor	919nm – 971nm	60m
	10	Cirrus	1299nm – 1449nm	60m
	11	Shortwave Infrared	1471nm – 1757nm	20m
	12		1960nm – 2444nm	20m

Methods

The workflow of the classification is visualized in Fig. 3.

Preprocessing

To prepare the image for the classification, a spatial subset and a spectral subset are created. The spatial subset shows an overview of the study area of Barisal as well as the surrounding rural areas (Fig. A1). The spectral subset includes the above-mentioned (Tab. 1) Sentinel-2 bands (Band 2, 3, 4, 5, 6, 7, 8, 8A, 11, 12). Subsequent, all image bands with 20m resolution are resampled to a 10m spatial resolution to keep the information of the higher resolution 10m bands.

Classes and Training Areas

The purpose of the land-use classification is to derive information on urban settlement structures. Accordingly, the two classes “Urban" and "Rural Settlements" are used for the description of these structures. “Agriculture" and "Bare Soil" are chosen to describe the undeveloped areas in general. Water areas are represented by the class "Water".

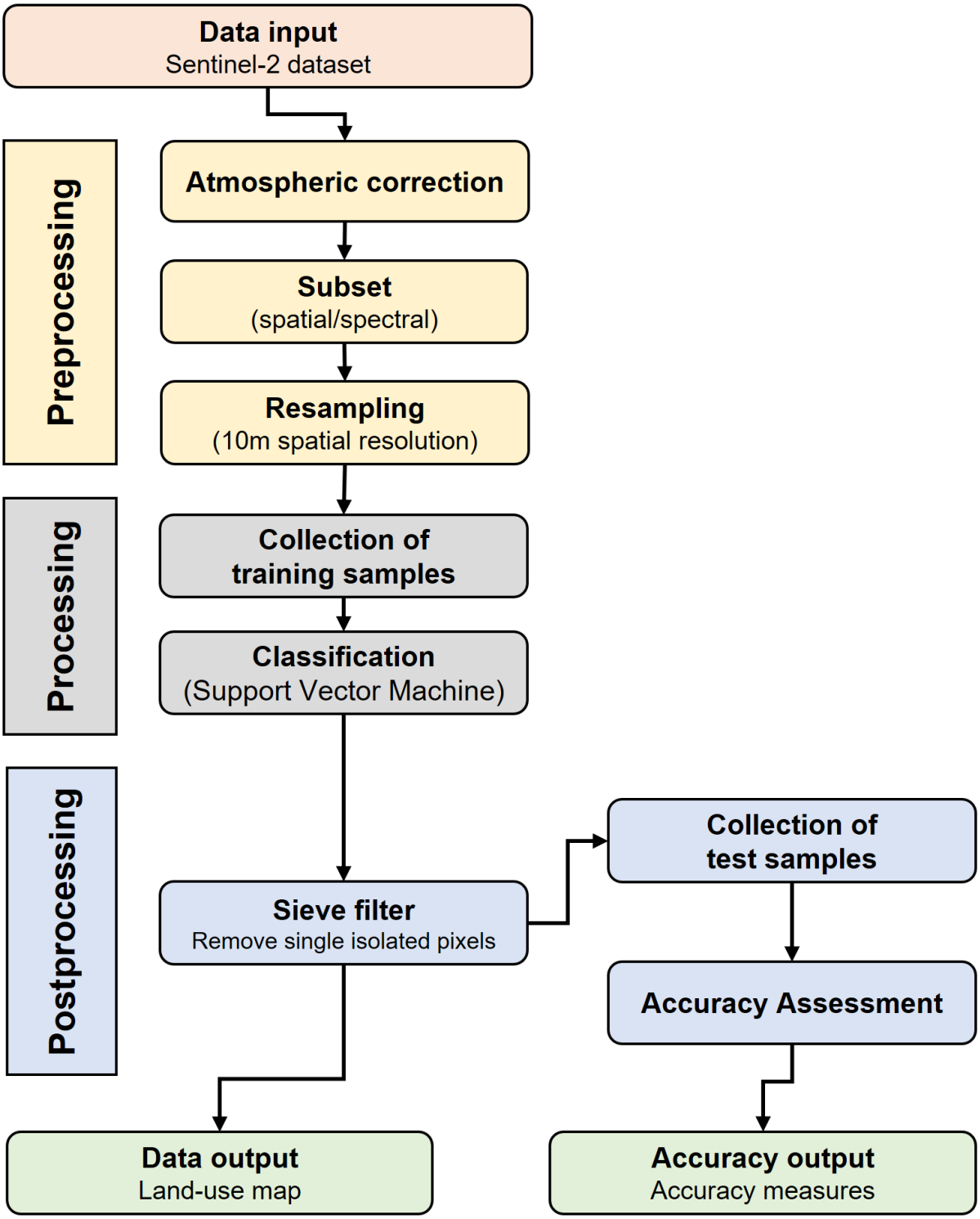

Figure 3: *Workflows of the Land-use classification.*

These classes are based on the CORINE Landcover (CLC) program (EUROPEAN ENVIRONMENT AGENCY, 2019). CORINE Landcover is a program of the European Commission to standardize the most important forms of land cover for environmental policy development. The standardized classes are based on biophysical characteristics of the Earth's surface (EUROPEAN ENVIRONMENT AGENCY, 2017).

"Water" includes all open water bodies, such as river, canals, channels, lakes and ponds. "Bare Soil" includes all surfaces of bright bare soil, such as riverbanks, pointbars and filled areas for urban development. "Urban" includes residential and industrial buildings without tree cover. Furthermore, it includes streets, railway lines and sealed surfaces. "Rural Settlements" include the city suburbs and rural villages that have tree coverage. "Agriculture" are all areas of farmland, such as cropland (rice, vegetables, etc.) or pasture land (for cattle, goats, etc.).

Training areas for all classes are selected from the Sentinel-2 dataset (see Tab. 2). To receive an acceptable classification result, the training areas must be both representative and complete for their land-use classes (LILLESAND ET AL., 2015).

All land-use classes have non-uniform spectral characteristics in common. For example, in the "Urban" class, the spectral characteristics of tin shacks and high-rise buildings differ. The "Agriculture" class includes spectral characteristics of different crops and in the "Water" class, different water qualities also differ spectrally. Different soil types in the "Bare Soil" class also have different spectral characteristics. The "Rural Settlements" class contains areas with different tree species, which result in different spectral characteristics.

The training areas of the land-use classes are required to represent these different spectral characteristics. The number of training areas therefore depends on the spectral variability within a land-use class (see Tab. 2).

The training areas are dispersed throughout the Sentinel-2 dataset to increase the representation of all variations in the land-use classes (LILLESAND ET AL., 2015).

Table 2: *Overview of the number of training areas per class.*

Class	Number of Training Areas
Agriculture	25
Bare Soil	10
Rural Settlements	10
Urban	15
Water	15

To show the spectral variabilities of the individual classes, the spectral profiles of the classes are shown in Fig. 4. Each curve represents the averaged spectral signatures of all training areas per class, based on the Sentinel-2 data set of 28.11.2019. Fig. 4 shows the spectral separability of the classes over the whole band range (see Tab. 1).

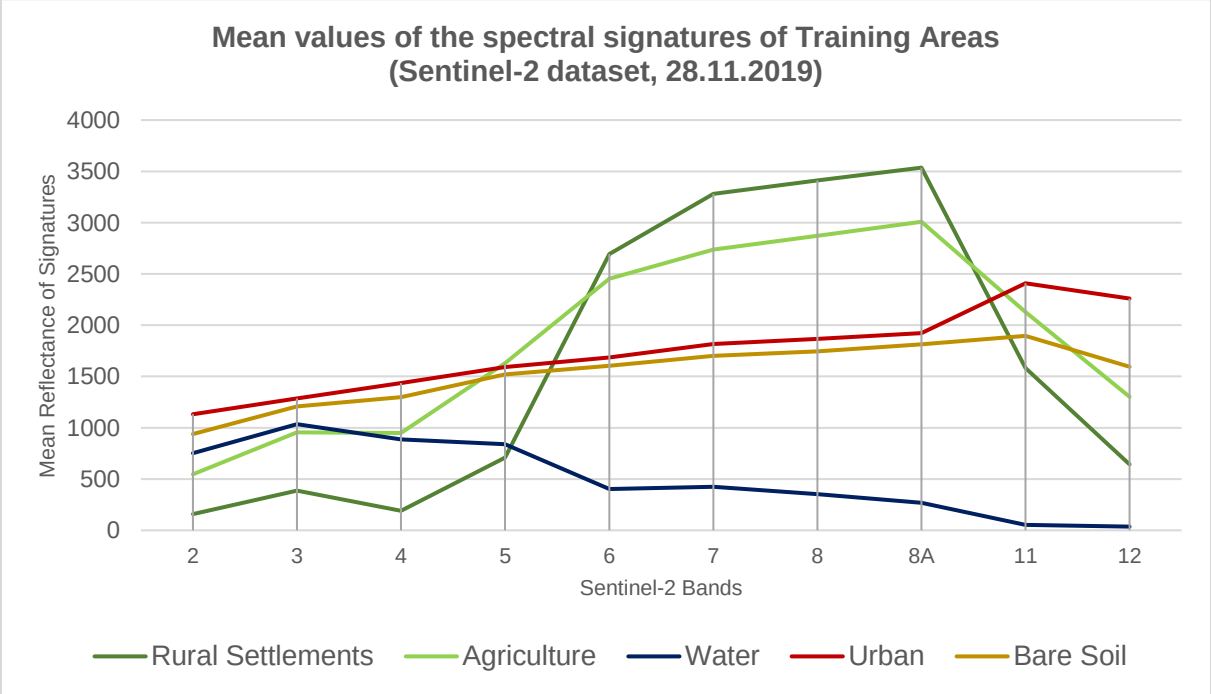

Figure 4: *Mean values of the spectral signatures of the training areas.*

The spectral curves of the classes “Agriculture” and “Rural Settlements” have similar spectral signatures. The reason for these similarities is that the class “Rural Settlements” is dominated by tree coverage and therefore represents a strong vegetation signal.

Both classes show vegetation-typical characteristics, such as the "red edge" (a significant increase of reflection in the near infrared bands 5 and 6 compared to the visible bands 2 to 4). The main differences are a higher reflectance of the class “Agriculture” in bands 3 to 5/11 and 12 and a higher reflectance of the class “Rural Settlements” in bands 6 to 8A.

The spectral signature of “Water” shows higher reflection values around band 6 to 8A leading to the interpretation that the water class/signature contains impurities, such as sediments. Pure water would have zero reflectance in these longer wavelengths.

The spectral signature of the class “Urban” shows a relatively continuous increase and is similar to the signature of “Bare Soil”. The main difference between both spectral signatures is a higher “Urban” reflectance in the shortwave-infrared compared to a lower reflectance of “Bare Soil” in this wavelength range.

Classification

To perform the supervised classification, the Support Vector Machine (SVM) classifier is selected, a method based on statistical learning theory. Support Vector Machines are supervised learning models with associated learning algorithms that analyze data used for classification.

The classifier looks at spectral boundaries between individual classes in the multidimensional feature space. It aims to find an optimal margin (known as “hyperplane”) to separate the classes. The data values that constrain the width of the margin are known as “support vectors” (JONES & VAUGHAN, 2010).

In its simplest form, a SVM separates two classes (a binary classifier). Nevertheless, a classification with multiple classes is possible. Based on the training areas, several binary classifiers are calculated which separate the properties of each class from those of every other class (known as “one-versus-one” approach). The number of binary classifiers depends on the number of classes to be separated:

$$n_{classifier} = \frac{n_{class} * (n_{class} - 1)}{2}$$

The variable $n_{classifier}$ represents the number of classifiers; the variable n_{class} represents the number of classes.

Therefore, the properties of the five classes of this investigation are separated using 10 binary classifiers (Tab. 3 shows an example of possible connections of classes), as a result the classes are differentiated spectrally. Each classifier designates a class name to every pixel, the most frequent class name assigns the pixel to the final class (RICHARDS, 2013).

Table 3: *The table shows all possible connections of classes (cf. RICHARDS, 2013).*

Number of binary classifiers	Class name 1	Class name 2
1	Agriculture	Bare Soil
2	Agriculture	Rural Settlements
3	Agriculture	Urban
4	Agriculture	Water
5	Bare Soil	Rural Settlements
6	Bare Soil	Urban
7	Bare Soil	Water
8	Rural Settlements	Urban
9	Rural Settlements	Water
10	Urban	Water

Post-Processing

The same object feature may be classified in different classes due to spectral variabilities. The classification result might show single isolated pixels of one class in the area of another class (LILLESAND ET AL., 2015).

To remove the single isolated pixels in the classification image, a sieve filter is applied. This filter replaces all pixel patches that are smaller than twelve pixels by the value of the surrounding neighbor class. A pixel patch is a group of pixels that share their sides or have connected angles. The final classification result is shown in Fig. A2 and A3.

Calculation of filled and non-filled areas

Based on the knowledge of the GSB colleagues and the experience gained during fieldwork, all urbanized areas and settlement structures in Barisal are developed on filled areas. Therefore, those areas are considered as filled areas, the classes “Urban” and “Rural Settlements” are reclassified to “Filled” and the classes “Water”, “Bare Soil” and “Agriculture” are reclassified to “Non-filled” (see Fig. A4).

Accuracy Assessment

During the accuracy assessment, randomly distributed test samples are used to compare the classification result with an independent high-resolution reference dataset. As a high-resolution reference dataset, free accessible Google Earth satellite images are used. Thus, details for a more precise interpretation of the actual land use become visible and the classification result can be assessed visually without having the necessity to collect ground truth information during fieldwork.

LILLESAND ET AL. (2015) recommends using at least 50 test samples per class for accuracy assessment. Following this recommendation, 250 test samples are randomly distributed in the image, using 50 samples for each class (Tab. 4).

Table 4: *Accuracy Assessment, Sentinel-2 dataset (28.11.2019).*

Sentinel-2, 28.11.2019		Reference						
		Agriculture	Bare Soil	Rural Settlements	Urban	Water	Row Total	**User's Accuracy (%)**
Classification	Agriculture	44	1	5	0	0	50	88.0
	Bare Soil	2	42	0	2	4	50	84.0
	Rural Settlements	3	0	46	1	0	50	92.0
	Urban	0	6	2	40	2	50	80.0
	Water	0	0	1	0	49	50	98.0
	Column Total	49	49	54	43	55	250	
	Producer's Accuracy (%)	89.79	85.71	85.18	93.02	89.09		
	Cohen's Kappa per Class	0.8	0.82	0.87	0.79	0.97		
	Overall Accuracy (%)	**88.4**						
	Overall Kappa	**0.86**						

Since the images from Google Earth represent a compilation of different points in time, the Sentinel-2 dataset is used as an auxiliary dataset. Both data sets were acquired at different stages of flooding. Therefore, the visual impression of the Sentinel-2 dataset is given priority over the data from Google Earth when assigning water areas. Based on these datasets, land-use classes are interactively assigned to the test sample classes. Following this, the test areas are compared with the classification results to receive the accuracy measures (Tab. 4).

The overall accuracy of the classification is 88.4 %. The Kappa coefficient, a measure for the agreement between classification result and reference shows a good result of 0.86. The User's Accuracy shows how reliable the classified pixels represent actual land use, while Producer's Accuracy shows how well an object class has been correctly classified. In addition, the Kappa coefficients of each class are displayed in order to individually evaluate the reliability of the classification result.
The “Water” class shows a User’s Accuracy of 98.0 % with a high corresponding Kappa coefficient of 0.97. The “Rural Settlements” (92.0 %) and the “Agriculture” (88.0 %) also show a high User’s Accuracy, compared to the classes “Bare Soil” and “Urban” with the lowest accuracies 84.0 % (“Bare Soil”) and 80.0 % (“Urban”). This is also visible in the Kappa coefficients, so that the agreement between the classification result and the reference data is 0.87 (“Rural Settlements”) and 0.8 (“Agriculture”) compared to 0.82 (“Bare Soil”) and 0.79 (“Urban”).

The reason for lower accuracy values of the classes “Agriculture”, “Bare Soil” and “Urban” (see Tab. 4) is related to different circumstances:
For example, the spectral signature of the class “Agriculture” shows similarities to the spectral signature of the class “Rural Settlements” (Fig. 4). Therefore, agricultural areas having similar spectral characteristics as the rural settlement areas may therefore be classified incorrectly and lead to a lower User’s Accuracy.
Table 4 also shows that four samples of “Bare Soil” were classified as “Water”. Fig. 4 already shows a higher reflection of water in bands 6 to 8A. This higher reflection and therefore the misclassification may be related to impurities (e.g. a higher sediment load) inside of the water bodies.
The lowest accuracy value (80.0 % User’s Accuracy) of the “Urban” class may be related to a mixed-pixel problem in the Sentinel-2 dataset. Individual residential or industrial buildings may be smaller than the resolution of the Sentinel-2 dataset (10m x 10m). As a result, a pixel represents a mixture of urban buildings and other surfaces (e.g. soil or trees). This mixture can lead to misclassification. Due to the high-resolution reference image, it is possible to interactively determine the main content of a pixel (e.g. urban buildings) and to assign it to the test sample classes. The mixed pixels of the Sentinel-2 dataset can thus lead to a lower accuracy in the "Urban" class.

The overall visual impression of the classification result (Fig. A2), as well as the overall accuracy and the overall Kappa coefficient (Tab. 4) show a good result and representation of the actual land-use.

2.2 River Shifting Change Detection Map

Rivers in Bangladesh are highly dynamic and underlie severe changes in location and intensity during a few years. During a few decades, rivers may change whole landscapes. The overall goal of this analysis is to provide information on the changes of the Meghna river system course and the direction of shifting. The river system includes the water bodies and pointbars. A regional map covers these changes from the area of Faridganj in the northeast to the area of Bauphal in the southwest (Fig. A5). Local changes inside this area are presented in a map showing only the city of Barisal (Fig. A16). The main focus is the mapping of present areas of the river system and former areas which were active in the past decades but are inactive recently. River course maps are provided for six time slices (1973, 1980, 1990, 2000, 2010 and 2019) (Fig. A8-A13). The change detection map shows data of the time slices with the highest difference in river system areas (1973, 2000 and 2019) (Fig. A8-A13, A15). A map focusing on the Barisal study area shows present and former river system areas using all six time slices (Fig. A16).

Data

To carry out the analysis, cloud-free optical images from Landsat Multispectral Scanner System MSS, Landsat Thematic Mapper TM and Copernicus Sentinel-2 missions are used. These are available during the period of the Bangladesh dry season between October and April, and images from January and February are used in the analysis. A comparison between images of different years is only possible when the target features (e.g. water) can be identified in all the images by similar response signal. This can be ensured by using images of the same month in every year of the analysis.

Starting 1973, one image per decade is used (1973, 1980, 1990, 2000, 2010 and 2019). To enable comparability between the final river shifting products, only bands from the Landsat and Copernicus Sensors with similar wavelengths positions have been chosen for processing (see Tab. 5 and Annexure C: Data).

Table 5: *Overview of the satellite images and their bands used for the analysis (EUROPEAN SPACE AGENCY 2017; UNITED STATES GEOLOGICAL SURVEY n.d.).*

Mission	**Sensing Date**	**Bands (B), Spatial Resolution/ Wavelengths**	
		Green	**NIR**
Landsat MSS	02.02.1973	B4, 60m 0.5-0.6 µm	B7, 60m 0.8-1.1 µm
	02.02.1980		
Landsat TM	07.01.1990	B2, 30m 0.52-0.6 µm	B4, 30m 0.76-0.90 µm
	19.01.2000		
	30.01.2010		
Sentinel-2	01.02.2019	B3, 10m 0.538-0.583 µm	B8, 20m 0.76-0.97 µm

Methods

The workflow of the analysis is visualized in Fig. 5.

Atmospheric Correction

Different atmospheric conditions during the sensing times of the images can result in a different image feature of the physically same ground objects. Therefore, to enable the comparison between all the images, an atmospheric correction is mandatory. An atmospheric correction eliminates the atmospheric effects in an image and results in a surface reflectance image that characterizes the surface properties.

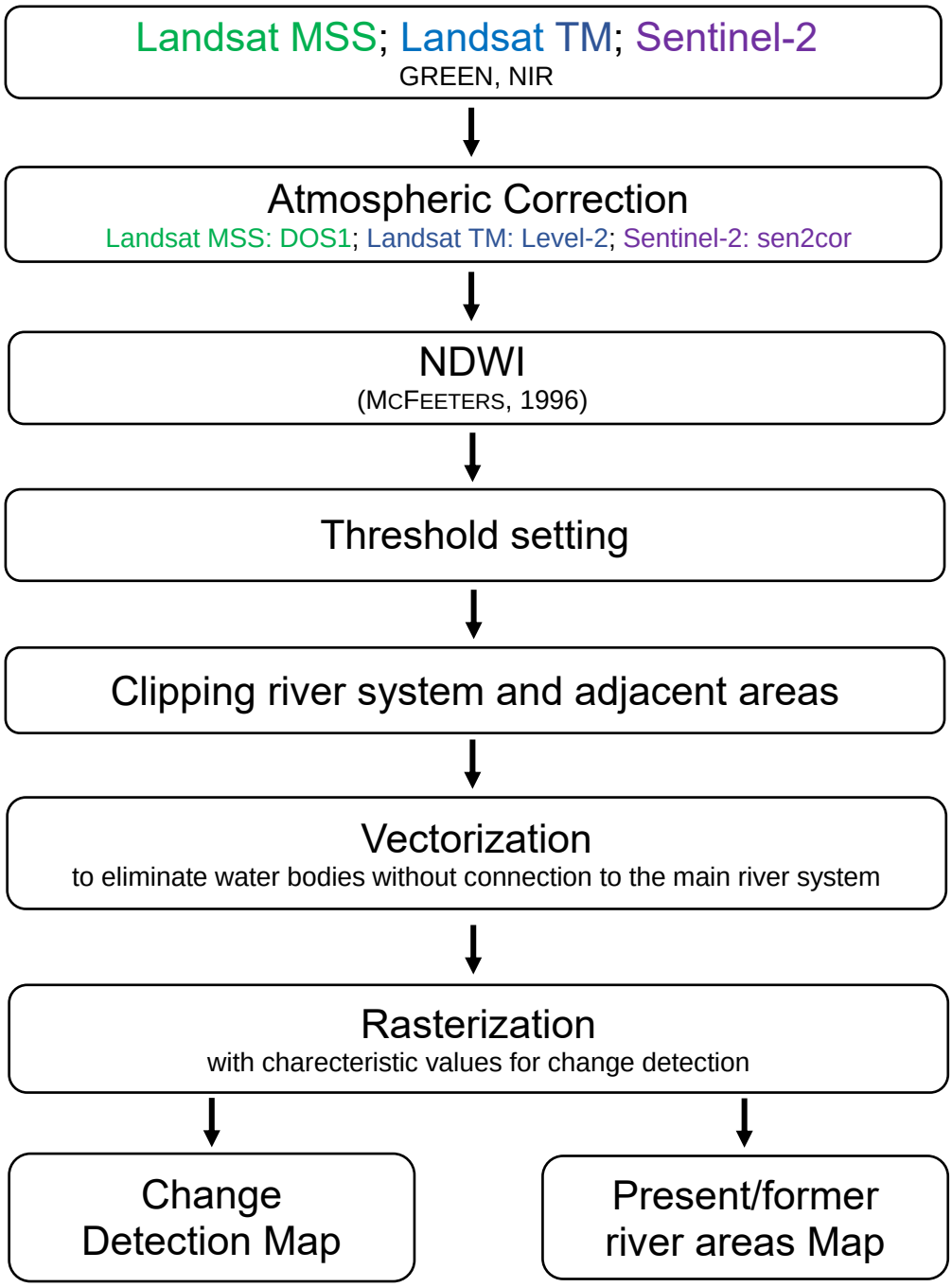

Figure 5: *Workflow of the River Shifting Change Detection analysis.*

Sentinel-2 and Landsat TM images are already atmospherically corrected and surface reflectance data are available for download (free Sentinel-2 download from Copernicus Open Access Hub and free Landsat TM download from USGS EarthExplorer).

The Sentinel-2 atmospheric correction is based on physical principals, physical-based algorithms use radiative transfer methods, which are simplified models of the radiation pathway from source to sensor, to model atmospheric scattering and absorption (LILLESAND ET AL., 2015). Auxiliary data such as water vapor data, atmospheric pressure or a digital elevation model are added to receive more precise information for the correction. The effects in the atmosphere are quantified by the model and used to calculate the surface reflectance values.

The Landsat TM surface reflectance "products are generated by a specialized software called Landsat Ecosystem Disturbance Adaptive Processing System (LEDAPS)" (LEDAPS PRODUCT GUIDE, 2020). Similar to the Sentinel-2 atmospheric correction, LEDAPS is also a physical-based algorithm that fits a radiative transfer model and includes auxiliary data to receive the atmospherically corrected surface reflectance product.

The Landsat MSS image is corrected by using the DOS1 (Dark Objects Subtraction) method. CHAVEZ (1996) describes that the methods "[…] basic assumption is that within the image some pixels are in complete shadow and their radiances [if above zero] received at the satellite are due to atmospheric scattering (path radiance). This assumption is combined with the fact that very few targets on the Earth's surface are absolute black, so an assumed one-percent minimum reflectance is better than zero percent." (CHAVEZ, 1996). The calculated radiance-value based on this assumption is used for the correction of the whole Landsat MSS image (image –based correction).

It is important to mention that the accuracy of an image-based correction technique is lower than a physically based correction (e.g. as applied for Sentinel-2) (CONGEDO, 2016). Nevertheless, CONGEDO (2016) states that image-based corrections "are very useful when no atmospheric measurements are available as they can improve the estimation of land surface reflectance" (CONGEDO, 2016).

Calculation of Normalized Difference Water Index (NDWI)

Using the respective bands of the images (Tab. 5), the NDWI is calculated (see Fig. A6). The Normalized Difference Water Index (NDWI) (MCFEETERS, 1996) uses the green and near-infrared bands to delineate open-water features.

Water surfaces show high reflections in the green and low reflections in the near-infrared wavelength region (see Fig. 6).

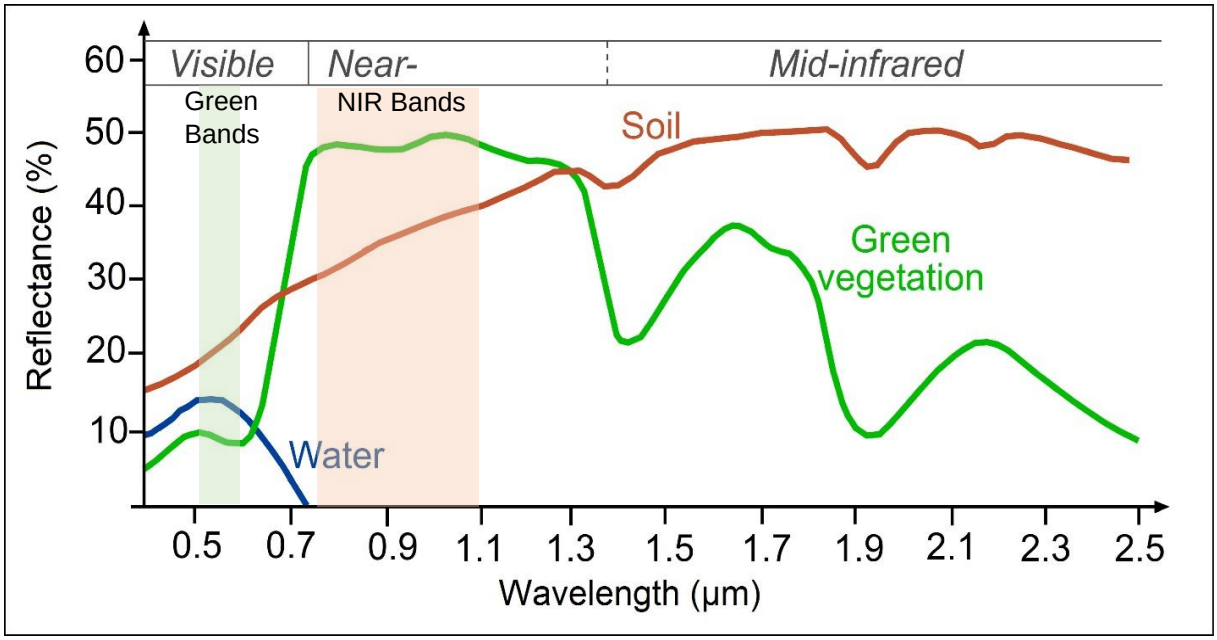

Figure 6: *Reflectance of water, soil and vegetation at different wavelengths; the wavelength areas used by the NDWI are highlighted in green (green bands) and red (NIR bands), modified after SEOS-PROJECT.EU, 2020.*

These differences are used to calculate an index that enhances the presence of open water features and suppresses the presence of soil and vegetation (McFeeters, 1996). The Waterindex is calculated as follows, using the respective bands of the satellite image:

$$NDWI = \frac{GREEN - NIR}{GREEN + NIR}$$

The generated index map contains values in the range of -1 to +1 (see Fig. A6), while excluding zero. Positive values are interpreted as water features. Soil and vegetation features have negative values (McFeeters, 1996).

Processing steps

At first, a threshold value is applied to discriminate between values that belong to the river system (water-bodies and pointbars) and all other values. This threshold value is defined manually by inspecting the pixels of the different NDWI images (see Tab. 6).

Table 6: *Thresholds to discriminate between river system and other values.*

NDWI image of the year	Threshold
1973	-0.25
1980	-0.2
1990	-0.06
2000	-0.08
2010	-0.03
2019	-0.15

The application of the thresholds results in maps that only show water-body and pointbar areas differentiated from other areas (see Fig. A7 as an example).

Based on these threshold maps, an area is clipped interactively (due to computing limitations of QGIS regarding data quantity) that covers mainly the river system (including water bodies and pointbars) and adjacent areas. In the next step, all remaining pixels of the river system in the clipped images are assigned the value “1”, whereas the areas below the threshold (see Tab. 6) are assigned NA.

The resulting image still includes many small objects that lie outside of the main riversystem (e.g. small ponds, agricultural canals). To eliminate these water bodies having no connection to the main river system, the raster data are vectorized and single isolated polygons are automatically eliminated, based on the assumption that the main river area shows in one connected polygon.

The results of all processed years are overlain to visualize the different extents (Fig. A8-A13). The three results with the greatest differences in extent are selected interactively and then processed for the change detection map: years 1973, 2000 and 2019 (Fig. A15).

Change Detection Map

The goal of the change detection map is to provide information on the changes of the Meghna river system course and the direction of shifting. The changes are visualized in a single map. The conversion of the vector map (polygons) back to a raster map enables to present different river areas with characteristic values in a single map.

A unique year-dependent characteristic value is assigned to the cells of each new raster image (see Tab. 7). The raster cell size is set to 20 m, as this is the pixel size, needed by the successive project analyses.
The yearly products are joined to receive the change detection map of the area of the Meghna river system for the different years (see Tab. 8).

Table 7: *Overview of the characteristic values per year.*

	1973	**2000**	**2019**
Characteristic value	1	10	100

Table 8: *Legend of the raster values in the change detection map.*

Raster value	**Area of the Meghna river system in**
1	1973
10	2000
11	1973, 2000
100	2019
101	1973, 2019
110	1973, 2000
111	1973, 2000, 2019

Mapping present and former river system areas
In the Barisal study area, the information of all results (1973, 1980, 1990, 2000, 2010, 2019) are included into a map that presents present and former areas of the Meghna river system.

Present areas are defined as the area of the Meghna river system in 2019.

Former areas are defined as the area of the Meghna river system in all years before 2019 but not in 2019.

The polygons of each year are rasterized. A unique year-dependent characteristic value is assigned to the cells of each new raster image (see Tab. 9). The raster cell size is set to 20 m, as this is the pixel size, needed by the successive project analyses.

The individual results are joined. The values of the map represent the area of the Meghna river system in different years (see Tab. 10). To reduce the values to present or former areas, the raster is reclassified into two classes (see Tab. 10). Areas where the river is not classified in 2019, are defined as former and are assigned with a value of “1”. Areas, which show the river system in 2019, are defined as present and are assigned with the value of “2”.

Table 9: *Overview of the characteristic values per year for the mapping of present/ former river system areas.*

	1973	**1980**	**1990**	**2000**	**2010**	**2019**
Characteristic value	1	10	100	1000	10000	100000

Table 10: *Legend of the raster cell values in the map of present/former river system areas.*

Characteristic value	**Area of the Meghna river system in**	**Reclassified value (1=former/2=present)**
1	1973	1
10	1980	1
11	1973, 1980	1
100	1990	1
101	1973, 1990	1
110	1980, 1990	1
111	1973, 1980, 1990	1
1000	2000	1
1001	1973, 2000	1
1010	1980, 2000	1
1011	1973, 1980, 2000	1
1100	1990, 2000	1
1101	1973, 1990, 2000	1
1110	1980, 1990, 2000	1
1111	1973, 1980, 1990, 2000	1
10000	2010	1
10001	1973, 2010	1
10010	1980, 2010	1
10011	1973, 1980, 2010	1

10100	1990, 2010	1
10101	1973, 1990, 2010	1
10110	1980, 1990, 2010	1
10111	1973, 1980, 1990, 2010	1
11000	2000, 2010	1
11001	1973, 2000, 2010	1
11010	1980, 2000, 2010	1
11011	1973, 1980, 2000, 2010	1
11100	1990, 2000, 2010	1
11101	1973, 1990, 2000, 2010	1
11110	1980, 1990, 2000, 2010	1
11111	1973, 1980, 1990, 2000, 2010	1
100000	2019	2
100001	1973, 2019	2
100010	1980, 2019	2
100011	1973, 1980, 2019	2
100100	1990, 2019	2
100101	1973, 1990, 2019	2
100110	1980, 1990, 2019	2
100111	1973, 1980, 1990, 2019	2
101000	2000, 2019	2
101001	1973, 2000, 2019	2
101010	1980, 2000, 2019	2
101011	1973, 1980, 2000, 2019	2
101100	1990, 2000, 2019	2
101101	1973, 1990, 2000, 2019	2
101110	1980, 1990, 2000, 2019	2
101111	1973, 1980, 1990, 2000, 2019	2
110000	2010, 2019	2
110001	1973, 2010, 2019	2
110010	1980, 2010, 2019	2
110011	1973, 1980, 2010, 2019	2
110100	1990, 2010, 2019	2

110101	1973, 1990, 2010, 2019	2
110110	1980, 1990, 2010, 2019	2
110111	1973, 1980, 1990, 2010, 2019	2
111000	2000, 2010, 2019	2
111001	1973, 2000, 2010, 2019	2
111010	1980, 2000, 2010, 2019	2
111011	1973, 1980, 2000, 2010, 2019	2
111100	1990, 2000, 2010, 2019	2
111101	1973, 1990, 2000, 2010, 2019	2
111110	1980, 1990, 2000, 2010, 2019	2
111111	1973, 1980, 1990, 2000, 2010, 2019	2

Results and Discussion

The resulting maps are added in Annexure A (A5-A16) and described in this section. For better orientation, topographical information and some in Bangladesh well-known cities are included in the final map visualization of the remote sensing based products.

Extent of the Meghna river system and its water body

As already mentioned, the NDWI values greater than the threshold lead to the classification of a larger area than just the water bodies as it includes water bodies and pointbars. All together is interpreted as full extent (maximum water coverage) of the Meghna river system based on discussions with the GSB colleagues. As an example, Figure A14 shows the NDWI result for 2019 with a threshold greater than -0.15 overlain on the Sentinel-2 RGB 432 image from 2019. It is visible that the water body and pointbars are included into the result.

Figure A8 to A13 show in blue the extents of the Meghna river system (based on NDWI) in the years of 1973, 1980, 1990, 2000, 2010 and 2019.

The different levels of details between the final maps are caused by the different spatial resolutions of the images. Due to the higher spatial resolution, Sentinel-2 shows more details than Landsat TM and Landsat MSS (Tab. 5).

It can be summarized, that the general shape of river system for the different years is visible in all decades.

Change Detection Map

Based on the NDWI evaluations, the change detection map is calculated (Fig. A15). This map includes information on the shifting direction of the river system, together with the locations of land-loss and possible land-gain. Furthermore, it shows which regions were part of the river system for the period between 1973 and 2019 (Fig. A15, dark blue).

In several regions of the river areas, changes in time are observable (Fig. A15):

Section A shows the relocations of several rivers west of the Meghna River. A major change here is the formation of numerous meander bows over the last decades. Turquoise color indicates the location of the river system in 1973; light orange shows it in the year 2000, dark orange in both years of 2000 and 2019. Red color indicates the position of the river system in 2019 only. In several meandering bows, the color sequence turquoise-light orange-orange-red can be seen. This sequence exhibits the continuous erosion of the river into one direction. For Section A (Fig. A15), it can be stated that this area of the Meghna River system due to erosion in numerous sections of the river system has developed into a more meandering system over the past few decades. As a result, from today's perspective, there are numerous former riverbeds that are now used for agriculture or have been integrated into the settlement area. Such former riverbeds and their current use should be evaluated for suitability when developing new urban areas.

A comparable, but considerably larger shift is evident in section B. Here, the river shifts over the decades towards the north, visible in the color sequence turquoise-light orange-orange-red. It is obvious that the location of the river in 1973 (shown in turquoise) is clearly separated from the current (2019) location of the river (shown in orange and red). Compared to a 2019 Sentinel-2 satellite image (see Fig. A5), it can be stated that agricultural and village settlement structures have developed in this area. This is evident from the dark green tree structures characteristic of rural settlements (see Fig. A5, section B). Together with the results from section A, it can be concluded that former riverbeds are reused for agriculture or settlement within a few years after riverbed relocation.

Section C shows a large-scale erosion surface that developed between the years 2000 and 2019 (see Fig. A15). A dark blue part of the Meghna River is visible in the western

part of the section. This color shows that the river was at this same location during all time slices (1973, 2000, and 2019). Immediately to the east, a narrow orange-colored stripe is visible, defining the position of the river in 2000 and 2019. The large red area to the east shows the position of the river in 2019. The dark blue-orange-red sequence exhibits that the river has moved significantly in the north-eastward direction within two decades (2000 - 2019).

Section D shows a shifting of the Meghna River to the south-west (Fig. A15). The dark blue-orange-red sequence, which is visible from the center of the section to the south-west, indicates a constant erosion after 1973. It is visible that the orange area is wider than the red area. That shows the erosion of a larger area until the year 2000 compared to the erosion of a smaller area shown in red until the year of 2019.

Overall the sections C and D show an erosion-driven growth of the south-eastern region of the Meghna River. This growth movement can be observed at both the eastern and the western riverbanks within the decades since 1973 (Fig. A15).

In summary, the Change Detection Map in Figure A15 shows significant changes of the Meghna river system between the years of 1973 and 2019.
Of particular note is that most former riverbeds are used for agriculture and settlement development. If these areas should be considered as development sites for a future urbanization, the shifting history of the river system must be assessed as part of a suitability analysis.

Present and former river areas in the Barisal study area
In the Barisal study area, the change detection map shows present and former areas (Fig. A16). The map allows locating areas of sedimentation processes (former areas) and provides indications on other geo-related processes (e.g. liquefaction-prone areas). West of the Kirtonkhola River, close to the urban areas of Barisal, larger areas of former riverbed are visible, these areas should be evaluated for their suitability for urban development in Barisal.

2.3 Inundation Map

Due to climate change, Bangladesh is experiencing an increase in rural-urban migration movements. Therefore, the demand for safe building ground is very high. One result is an increasing lateral growth of urban areas. However, urban growth is limited to suitable building ground and eligible areas are often low-lying and therefore prone to flooding during the yearly monsoon season between May and October. Planning agencies may benefit from geodata on inundation-prone areas that are reliable, available frequently and sustainable, easy to process and easily understandable.

The overall objective of this analysis is to receive a map that gives an overall impression on the frequency of inundation in areas that are at risk of flooding (Fig. A17) for the years 2015 to 2020. The analysis is carried out using 12 Sentinel-1 radar images from 2015 to 2020 and a threshold approach to differentiate between inundated and non-inundated areas. To ensure an easy processing of the large amount of multi-temporal radar data, the analysis is carried out using the online processing tool Google Earth Engine (see the programming code in Annexure B).

The Bangladesh Water Development Board (BWDB) already established inundation mapping using Sentinel-1 datasets. In their annual flood reports, the BWDB is using an inundation map to verify the output of a flood-forecasting model (BANGLADESH WATER DEVELOPMENT BOARD 2018, pp. 92-93).

The location of the city of Barisal on the Kirtonkhola River favors busy shipping traffic (see Fig. A20, sections A and B). In the radar images, shipping traffic is visible due to a different backscatter compared to the water surfaces (see Fig. A18, section A). Different man-made objects, like the Shaheed Abdur Rab Serniabat Bridge, are also visible due to a deviation from the water surface's backscatter. In Fig. A17 the shipping traffic and man-made objects differentiate as separated units in the inundation map.

Data

The analysis is based on Copernicus Sentinel-1 images starting 2015, with operation of the Sentinel-1 sensor.

Google Earth Engine states to preprocess the images using the Sentinel-1 Toolbox to receive radiometrically calibrated images, terrain corrected and thermal noise removed (GOOGLE EARTH ENGINE DATA CATALOG, 2020).

A data selection from the rainy season in Bangladesh is required to map the maximum inundation. The selected images are acquired in “IW” (interferometric wide swath), the default acquisition mode of Sentinel-1 (EUROPEAN SPACE AGENCY, 2020). To differentiate between water and non-water pixels, the VH polarization is selected. Preliminary works in the study areas have shown that VH is the most suitable polarization for the detection of water. The respective spatial resolution of the VH polarization images is 10 meter.

The Bangladesh rainy season is roughly between May and October of each year. Depending on the year, the time of maximum inundation for the study area of Barisal is in the months between June and August (see Tab. 11). This assumption is based on the flood reporting by the BWDB (see e.g. BANGLADESH WATER DEVELOPMENT BOARD 2017, 2018, 2019) and by interactively assessing and selecting the images from a period that show the largest inundated areas. Since the exact dates of maximum inundation of a year are unknown, all available images of the respective months of each year are processed in this analysis.

Finally, using the above-mentioned benchmarks, 12 Sentinel-1 images of descending orbits are selected for the processing (e.g. Annexure B: lines 12-23). Annexure C: Data lists the images in a table.

Table 11: *Months of maximum inundation in the years 2015-2020.*

Year	Month(s) of maximum inundation
2015	July
2016	June
2017	August
2018	July
2019	July/August
2020	August

Method

The workflow of the processing in Google Earth Engine is visualized in Fig. 7. The selected images of each year are combined and mean values are calculated. The mean-value images are subsetted to fit the extent of the study area (see Fig. A18; Annexure B, lines 24-29).

Thresholding

Water surfaces appear in black and dark gray colors in the averaged amplitude images (see Fig. A18). In order to identify a threshold value, the values of assumed water and non-water image areas are identified interactively. Based on experience in the definition of thresholds discriminating between water and non-water surfaces, the identified threshold values in Bangladesh range from -20 dB to -22 dB. For the Barisal study area, a threshold value including values smaller than -21 dB is chosen and applied to images from all years (Annexure B, lines 109-118). The output image only shows pixels smaller than the threshold, representing the inundated areas of each year (see Fig. A29).

All areas that have been inundated between 2015 and 2020, are compiled by combining the threshold images of all years into one image (see Fig. A17; Annexure B, lines 120-122). The result is exported with a 20m spatial resolution, which is a requirement for further analyses in the project (Annexure B, lines 128-140).

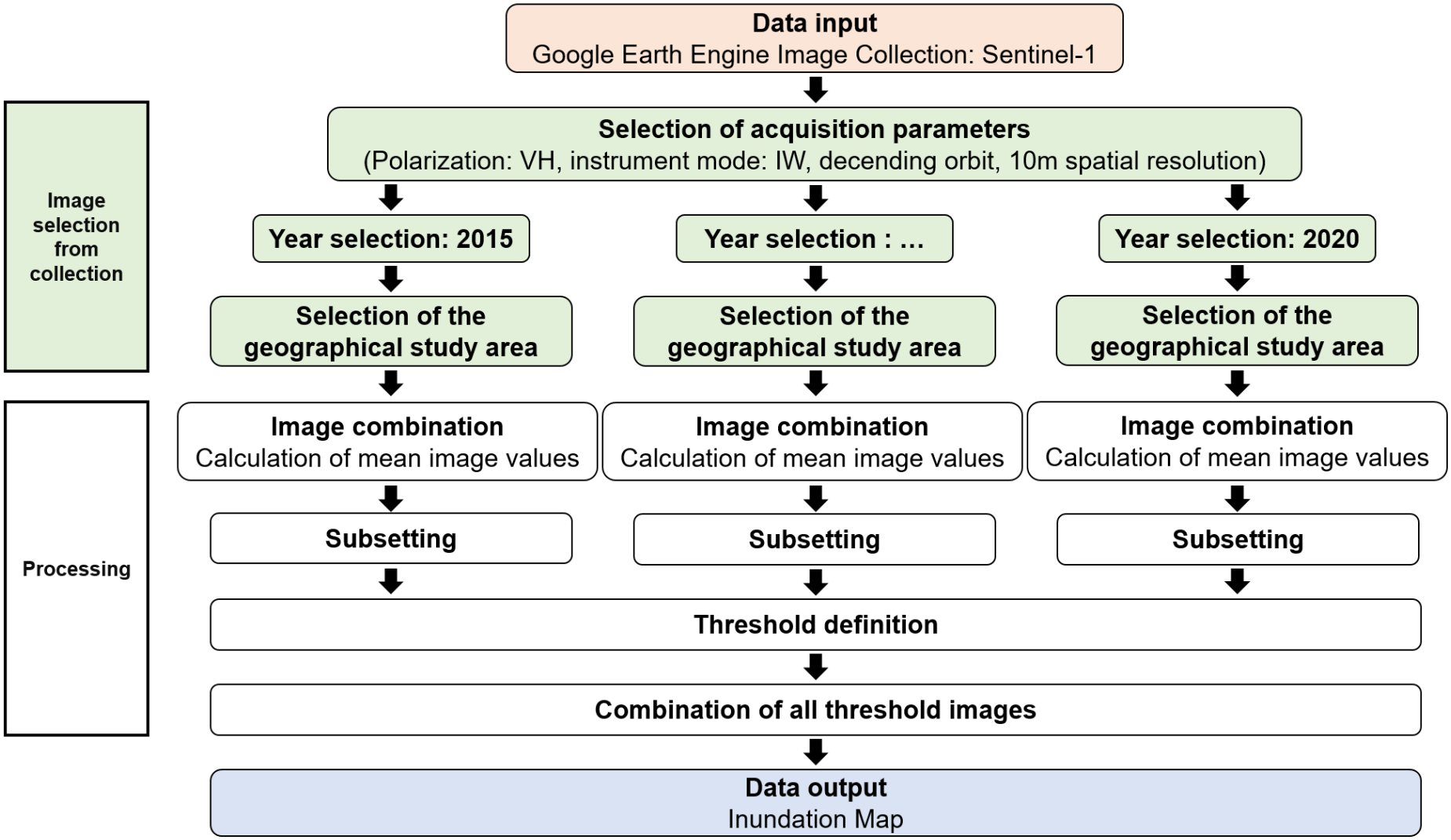

Figure 7: *Workflow of the Google Earth Engine processing of the inundation mapping method.*

Results and Discussion

The resulting map presents the areas and frequencies of inundation between 2015 and 2020 (see Fig. A17).

The map exhibits three major areas: (1) The city area of Barisal, west of the Kirtonkhola river which only shows rarely inundated areas in the years from 2015-2020. (2) The rural area that stretches west of the city of Barisal in a north-south direction and shows frequent inundation and less frequent inundation further inland compared to areas near the river. (3) Frequently inundated areas in the south around Barisal University, east of the Kirtonkhola River.

Many small areas in the Barisal city area are inundated yearly, representing ponds and lakes as they partially overlap with the water bodies in the topographic base map (data of the Survey of Bangladesh and OpenStreetMap). Nevertheless, the majority of frequently inundated areas is located in the outskirts of Barisal (see Fig. A17).

The rural agricultural areas in the west of Barisal city, which are not in close proximity to the rivers, have the lowest frequency of inundation (Fig. A17). These areas have been inundated once or twice during the study period between 2015 and 2020. The agricultural areas closer to the river show higher frequency of five to six times of inundation within the period between 2015 and 2020. (e.g. section A, Fig. A17). Figure 8 shows such an area that is used for rice cultivation during the dry season and is frequently inundated during the rainy season.

Figure 8: *Agricultural area in section A, View to the north-east. During the rainy season, the shown area is frequently inundated. Photo: L. Wimmer, 12/2018.*

Section B shows a floodplain, lying north of the Junhar River (see Fig. A17). Due to its natural proximity to the river, the floodplain shows a frequent inundation of three to six inundations between 2015 and 2020. The generally low-lying terrains, which are only slightly elevated above the river's water level, show also large inundated areas during the months outside of the rainy season (see Fig. 9; Fig. 9b exhibits inundation in the beginning of December 2018).

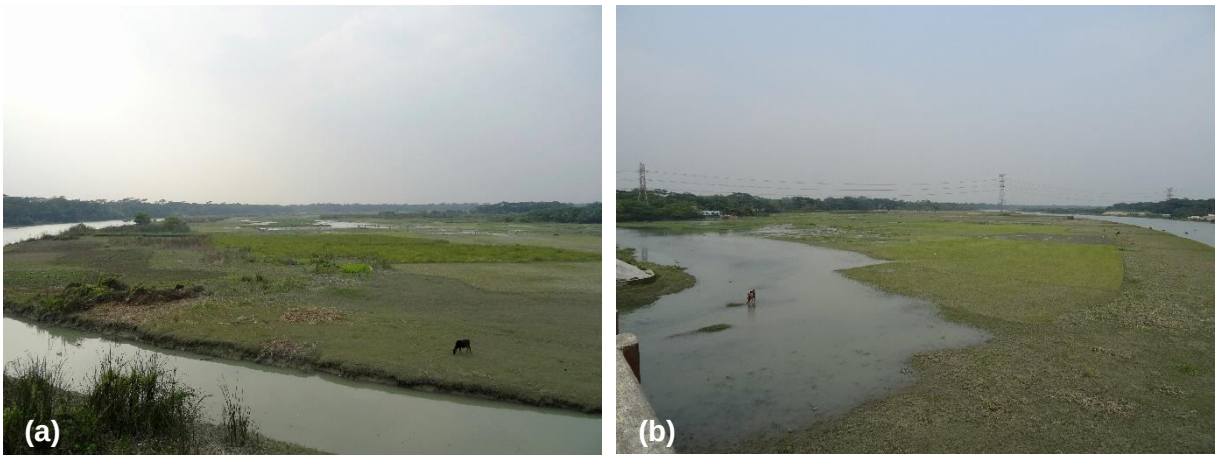

Figure 9: *Floodplain north of the Junhar River in section B that is frequently inundated during the rainy season. (a) View to the west; (b) View to the east. Photo: L. Wimmer, 12/2018.*

The analysis of the river shifting change detection shows that the area of today's floodplain in section B (Fig. A17, see also Figure 9) has been part of the water body of the Junhar River since 1973 (see chapter 2.2).

Immediately east of the urban area of Barisal at the riverbank on the Kirtonkhola River, section C exhibits an area that was inundated two to four times during the period of 2015 to 2020 (see Fig. A17, section C). Similar to the floodplain in section B, the analysis of the river shifting change detection revealed that this area was part of the Kirtonkhola River in earlier decades (see chapter 2.2). In today's times, this area is not a part of the River anymore, but is subjected to frequent inundation during the rainy seasons.

Section D shows the area around Barisal University (see Fig. A17, section D). The center of the section is characterized by less frequent inundation with one to two inundations during the study period. On the other side, areas near the Kirtonkhola River, were inundated more frequently – four to six times – during the study period. The southern part of section D shows a large frequently inundated area, which may occur due to the confluence of two rivers (see Fig. A17).

It can be concluded that between 2015 and 2020 for the rainy season mainly areas in the rural outskirts of Barisal were inundated. Additionally, areas near the rivers had a higher frequency of inundation during this period. Former parts of the rivers nowadays also show a higher inundation frequency.

References

BANGLADESH WATER DEVELOPMENT BOARD (2017): Annual Flood Report 2017. – <http://www.ffwc.gov.bd/images/annual17.pdf>. (Last access: 19.02.2021).

BANGLADESH WATER DEVELOPMENT BOARD (2018): Annual Flood Report 2018. – <http://www.ffwc.gov.bd/images/annual18.pdf>. (Last access: 16.12.2020).

BANGLADESH WATER DEVELOPMENT BOARD (2019): Annual Flood Report 2019. – <http://www.ffwc.gov.bd/images/annual19.pdf>. (Last access: 19.02.2021).

CHAMBELL J. B. (1996): Introduction to Remote Sensing. 2nd edition. Taylor & Francis. London.

CHAVEZ, P. S. (1996): Image-Based Atmospheric Corrections - Revisited and Improved. Photogrammetric Engineering and Remote Sensing. Vol. 62. No. 9. 1025-1036.

CONGEDO, L. (2016): Semi-Automatic Classification Plugin Documentation. – <http://dx.doi.org/10.13140/RG.2.2.29474.02242/1>. (Last change: n.d.). (Last access: 08.08.2019).

EUROPEAN ENVIRONMENT AGENCY (2017): Copernicus Land Service – Pan-European Component: CORINE Land Cover. <https://land.copernicus.eu/user-corner/publications/clc-flyer/at_download/file>. (Last change: n.d.). (Last access: 22.01.2021).

EUROPEAN ENVIRONMENT AGENCY (2019): Updated CLC illustrated nomenclature guidelines. - <https://land.copernicus.eu/user-corner/technical-library/corine-land-cover-nomenclature-guidelines/docs/pdf/CLC2018_Nomenclature_illustrated_guide_20190510.pdf>. (Last change: n.d.). (Last access: 22.01.2021).

EUROPEAN SPACE AGENCY (2017): Sentinel-2 Spectral Response Functions (S2-SRF). – <https://earth.esa.int/web/sentinel/user-guides/sentinel-2-msi/document-library/-/asset_publisher/Wk0TKajiISaR/content/sentinel-2a-spectral-responses>. (Last change: 19.12.2017). (Last access: 13.06.2019).

EUROPEAN SPACE AGENCY (2019): Sen2Cor Configuration and User Manual V2.8. – <http://step.esa.int/thirdparties/sen2cor/2.8.0/docs/S2-PDGS-MPC-L2A-SUM-V2.8.pdf>. (Last change: 05.02.2019). (Last access: 22.08.2019).

EUROPEAN SPACE AGENCY (2020): Sentinel-1 User Guide: Interferometric Wide Swath. <https://sentinel.esa.int/web/sentinel/user-guides/sentinel-1-sar/acquisition-modes/interferometric-wide-swath>. (Last change: n.d.). (Last access: 16.12.2020).

FORNARO, G., PASCAZIO, V. (2014): Chapter 20 - SAR Interferometry and Tomography: Theory and Applications. Academic Press Library in Signal Processing. Vol. 2. 1043-1117. doi: 10.1016/B978-0-12-396500-4.00020-X.

GOOGLE EARTH ENGINE DATA CATALOG (2020): Sentinel-1 SAR GRD: C-band Synthetic Aperture Radar Ground Range Detected, log scaling. – <https://developers.google.com/earth-engine/datasets/catalog/COPERNICUS_S1_GRD>. (Last change: n.d.). (Last Access: 16.12.2020).

JONES, H. G. AND VAUGHAN, R. A. (2010): Remote Sensing of Vegetation – Principles, Techniques, and Applications. Oxford University Press.

LILLESAND, T. M., KIEFER, W., CHIPMAN, J. W. (2015): Remote Sensing and Image Interpretation. Seventh Edition. Wiley.

MCFEETERS, S. K. (1996): The use of the Normalized Difference Water Index (NDWI) in the delineation of open water features. International Journal of Remote Sensing. Vol. 17. No. 7. 1425-1432.

MOREIRA, A., PRATS-IRAOLA, P., YOUNIS, M., KRIEGER, G., HAJNSEK, I., AND MUELLER-WILM, U., DEVIGNOT, O., PESSIOT, L. (2018): Level 2A Input Output Data Definition (IODD) v2.5.5. – <https://step.esa.int/thirdparties/sen2cor/2.5.5/docs/S2-PDGS-MPC-L2A-IODD-V2.5.5.pdf>. (Last change: 23.03.2018) (Last access: 20.05.2019).

PRASAD S., BRUCE L. M., CHANUSSOT J. (2011): Introduction. Optical Remote Sensing. Augmented Vision and Reality, Vol. 3. Springer. Berlin, Heidelberg.

Rencz A. N. (1999): Manual of Remote Sensing. 3rd edition, Vol. 3. Remote Sensing for the Earth Sciences. John Wiley & Sons.

RICHARDS, J. A. (2009): Remote Sensing with Imaging Radar. Springer-Verlag. Berlin, Heidelberg.

RICHARDS, J. A. (2013): Remote Sensing Digital Image Analysis – An Introduction. 5th edition. Springer. Heidelberg. New York. Dordrecht. London.

SABINS F. F. (1996): Remote Sensing. 3rd edition. Freemann and Company. New York.

UNITED STATES GEOLOGICAL SURVEY (n.d.): What are the band designations for the Landsat satellites? – <https://www.usgs.gov/faqs/what-are-band-designations-landsat-satellites>. (Last change: n.d.). (Last access: 13.06.2019).

UNITED STATES GEOLOGICAL SURVEY (2020): Landsat 4-7 Surface Reflectance (LEDAPS) Product Guide. Version 3.0. August 2020. – <https://prd-wret.s3.us-west-2.amazonaws.com/assets/palladium/production/atoms/files/LSDS-1370_L4-7_C1-

SurfaceReflectance-LEDAPS_ProductGuide-v3.pdf>. (Last change: August 2020). (Last access: 02.11.2020).

USTIN S. L. (2004): Manual of Remote Sensing. 3rd edition, Vol. 4. Remote Sensing for Natural Resource Management and Environmental Monitoring. John Wiley & Sons.

WOODHOUSE, I. H. (2006): Introduction to Microwave Remote Sensing. 1st edition. CRC Press. Boca Raton.

Annexure A: Maps

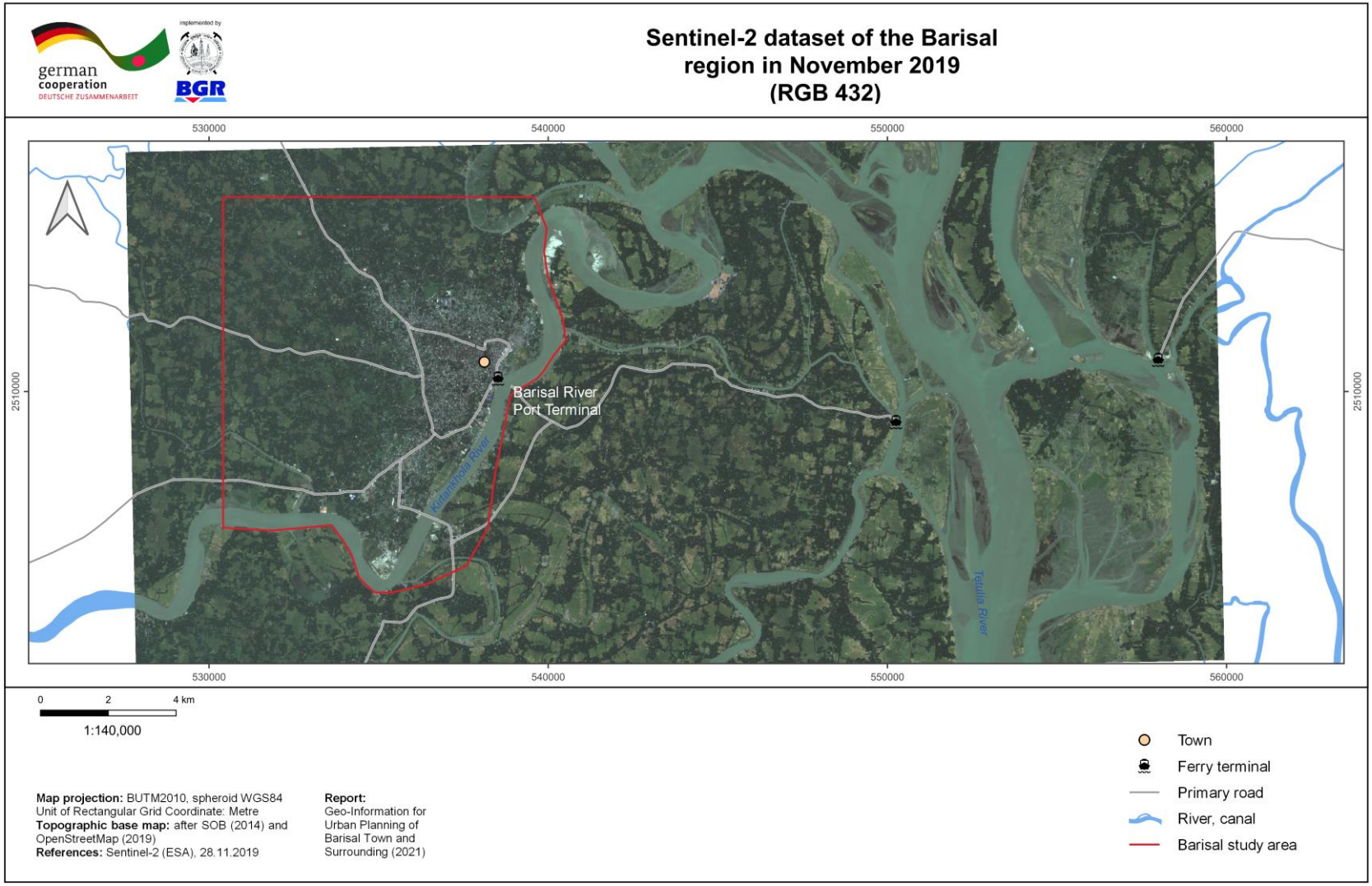

Figure A1: *Sentinel-2 Dataset of the Barisal Region, 18.11.2019 (RGB 4-3-2).*

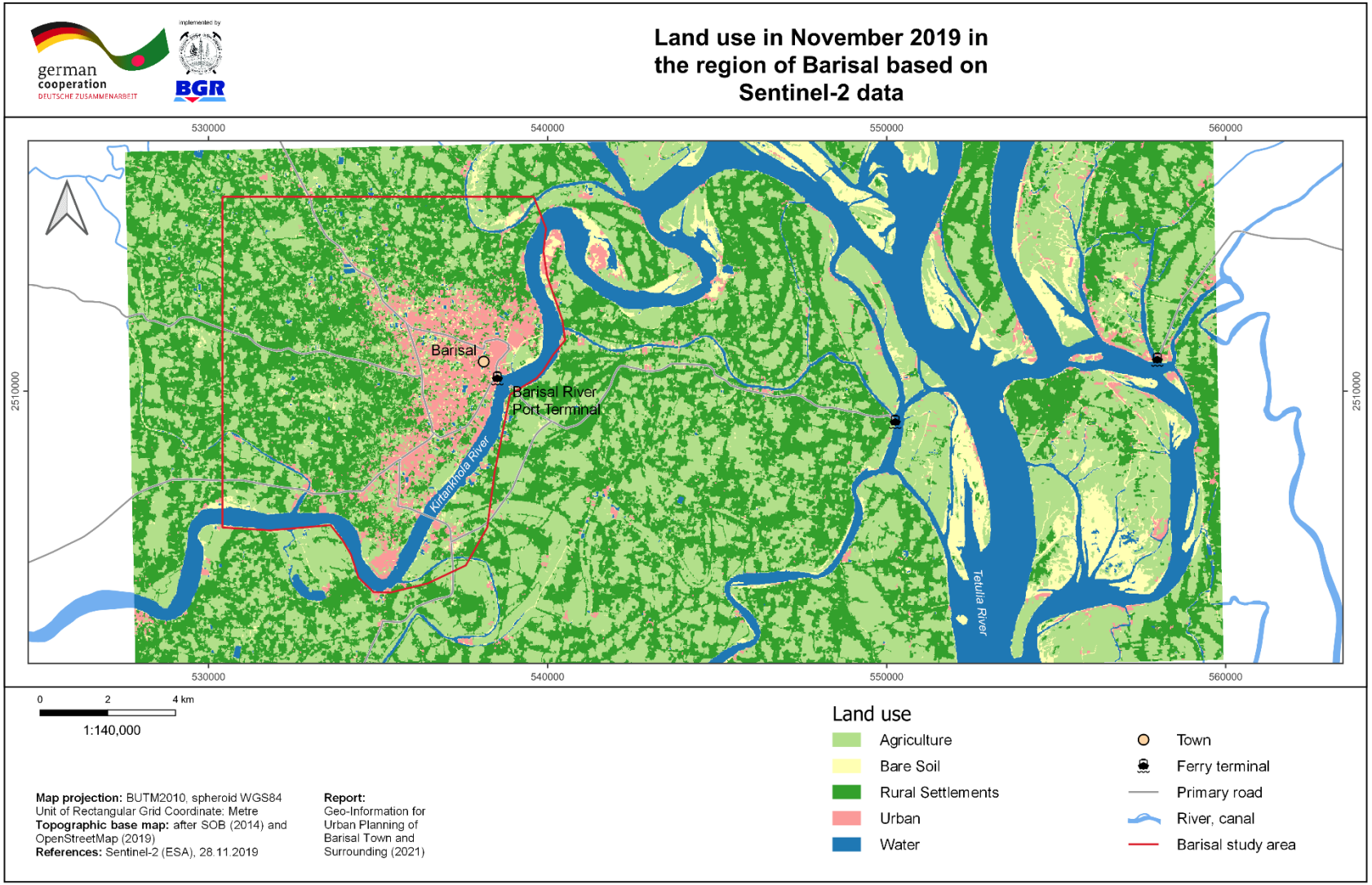

Figure A2: *Land use in November 2019 in region of Barisal based on Sentinel-2 data.*

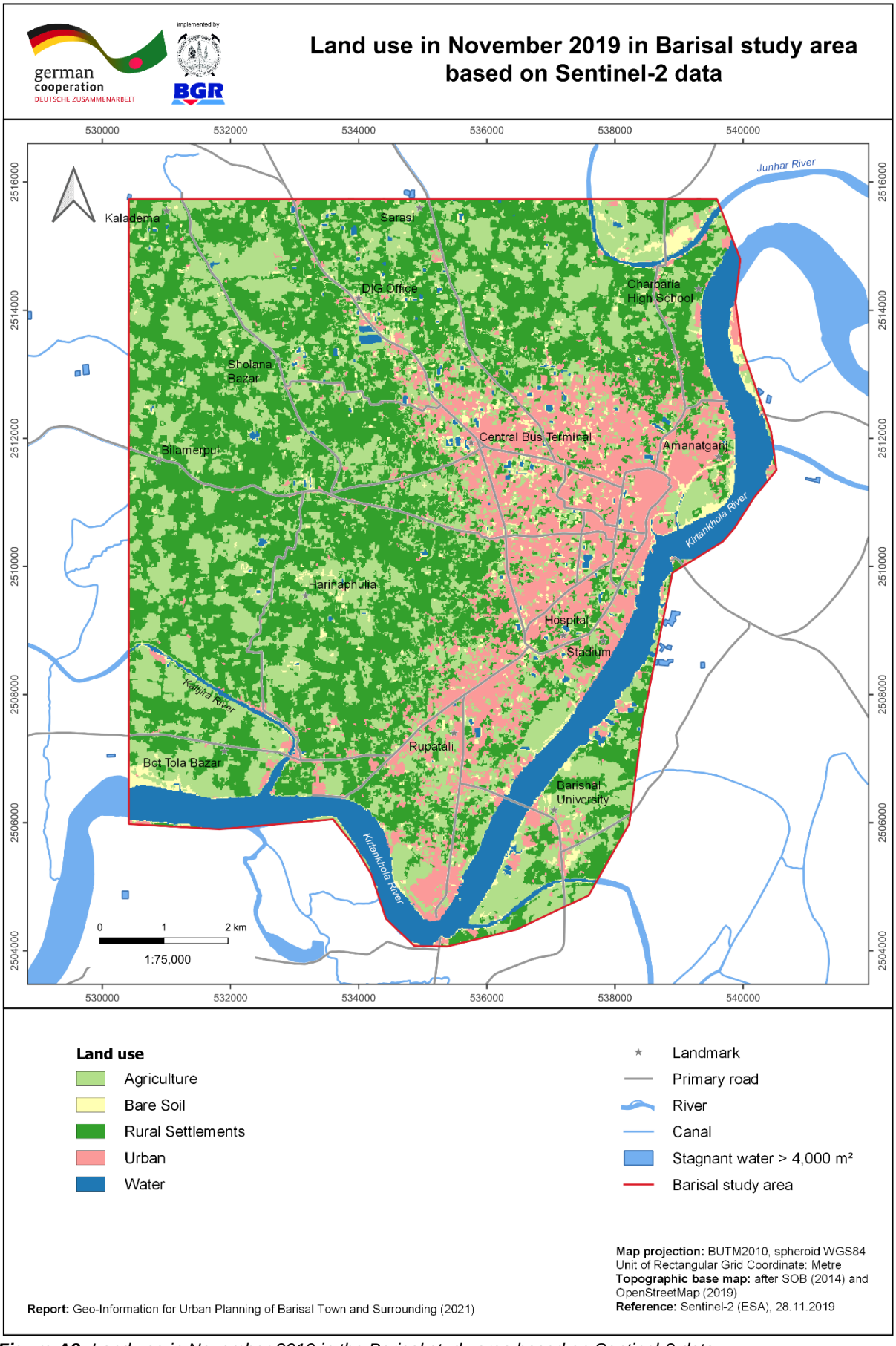

Figure A3: *Land use in November 2019 in the Barisal study area based on Sentinel-2 data.*

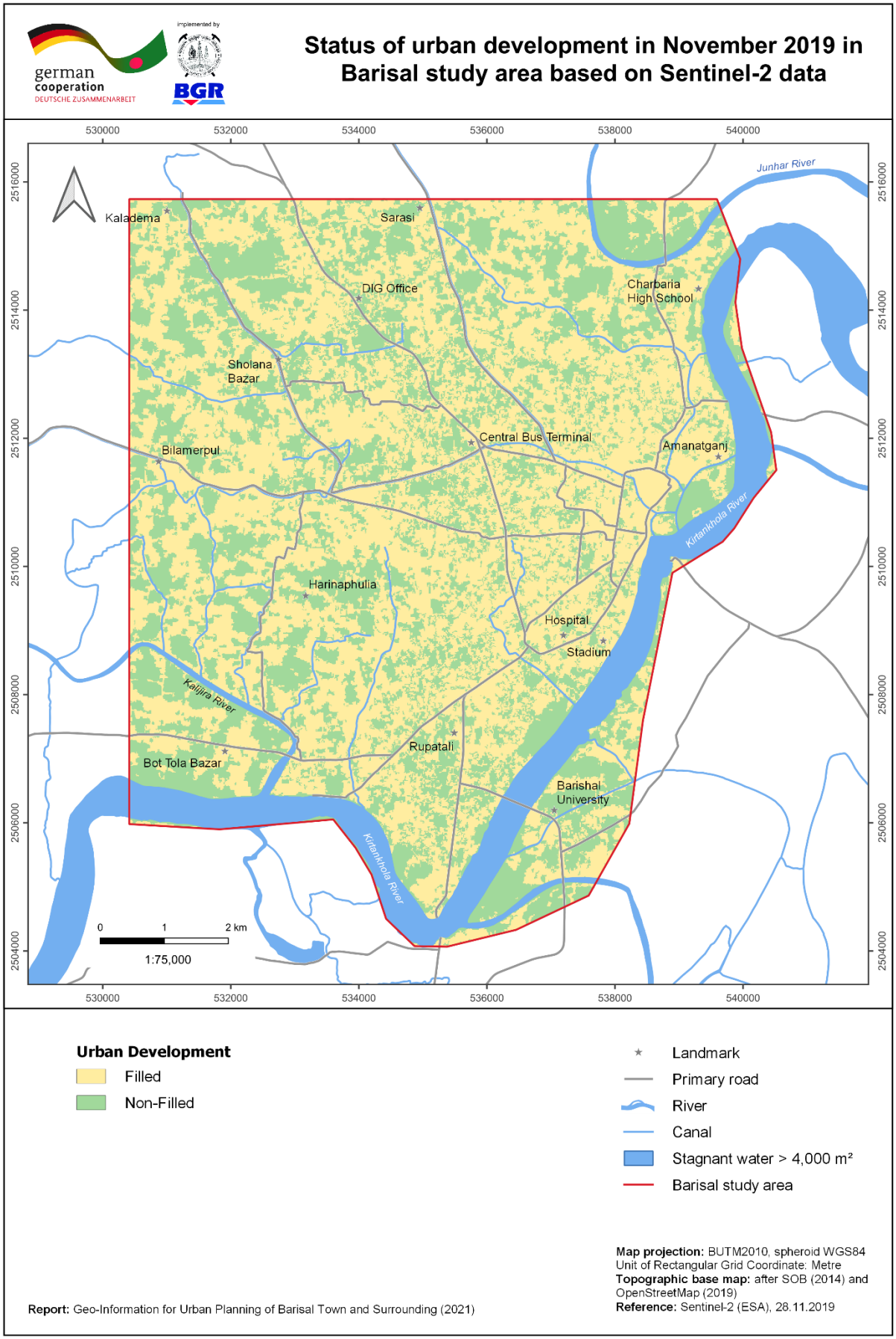

Figure A4: *Status of urban development in November 2019 in the Barisal study area based on Sentinel-2 data.*

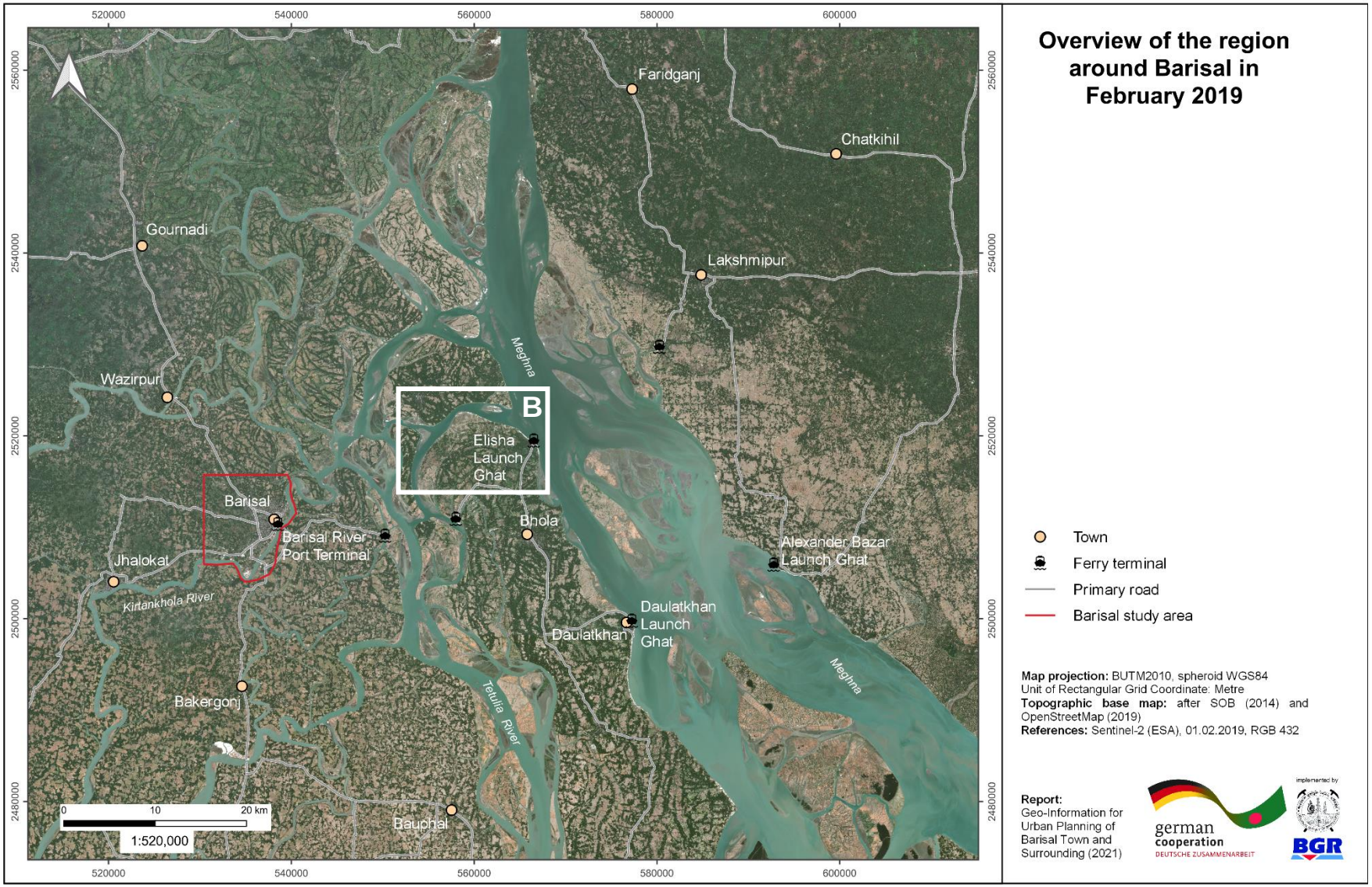

Figure A5: *Overview of the region around Barisal (Sentinel-2, RGB 432, 01.02.2019).*

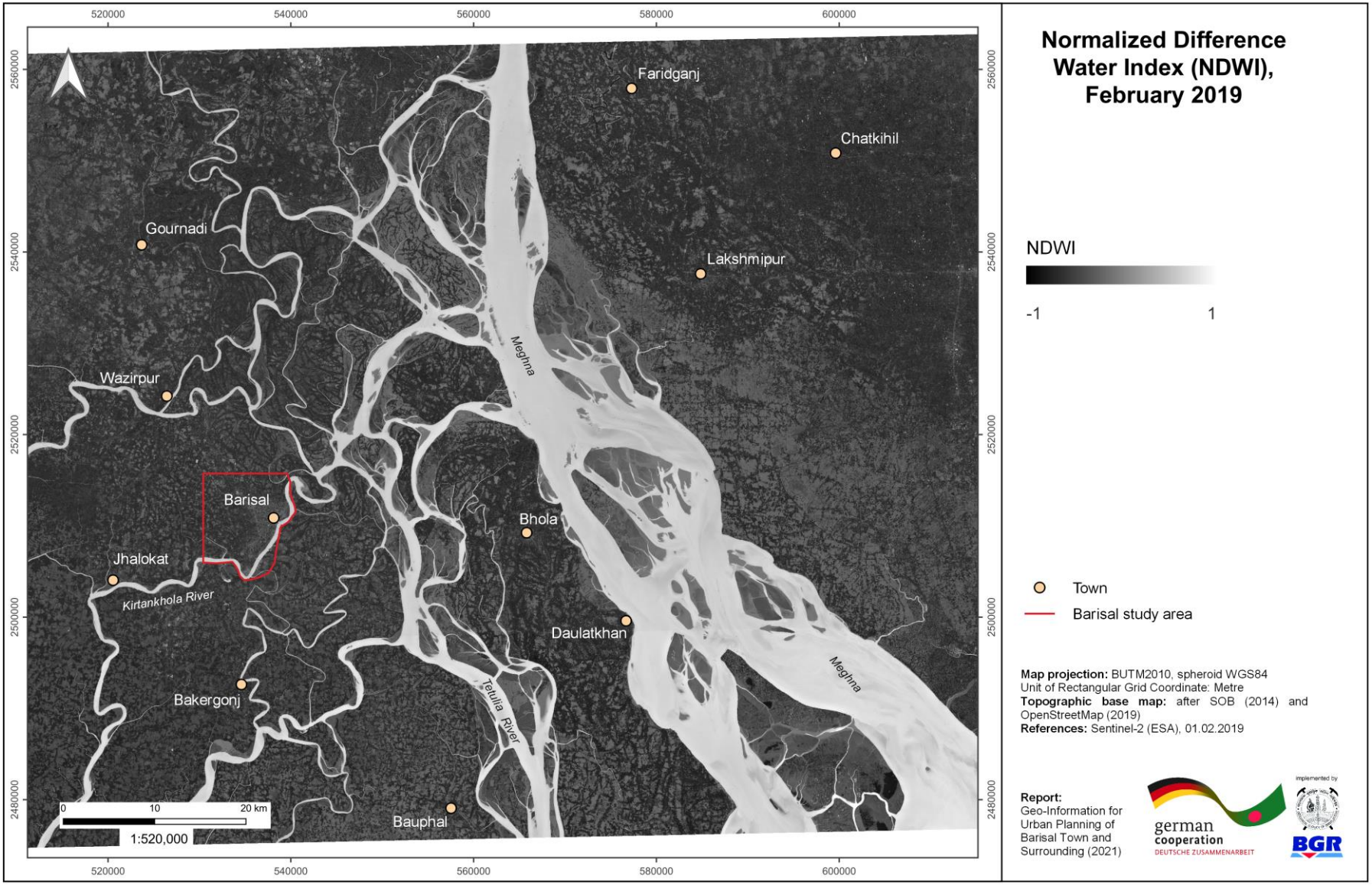

Figure A6: *Normalized Difference Water Index (NDWI), based on Sentinel-2 imagery (01.02.2019).*

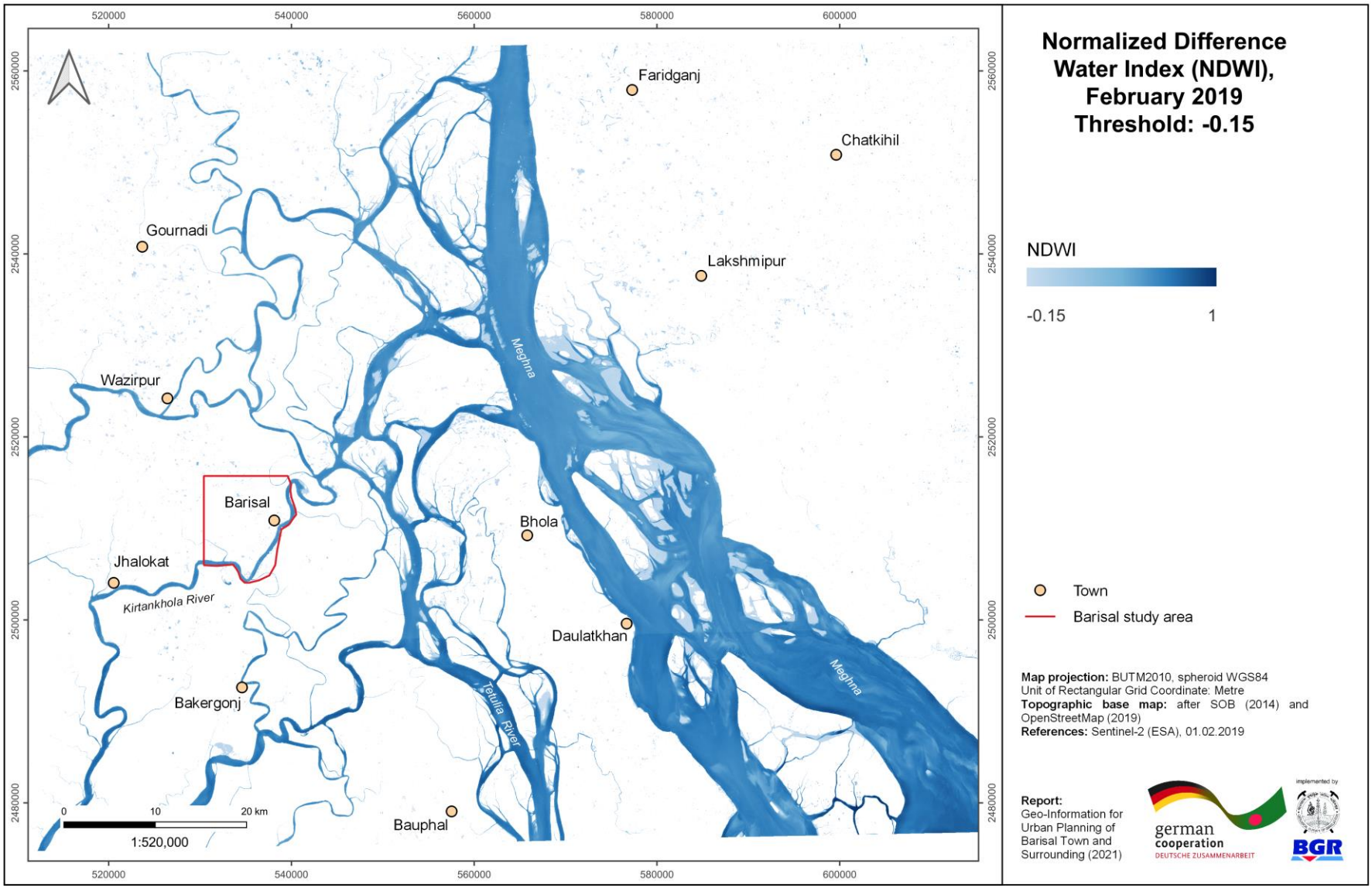

Figure A7: *Normalized Difference Water Index (NDWI), based on Sentinel-2 imagery (01.02.2019), threshold of -0.15.*

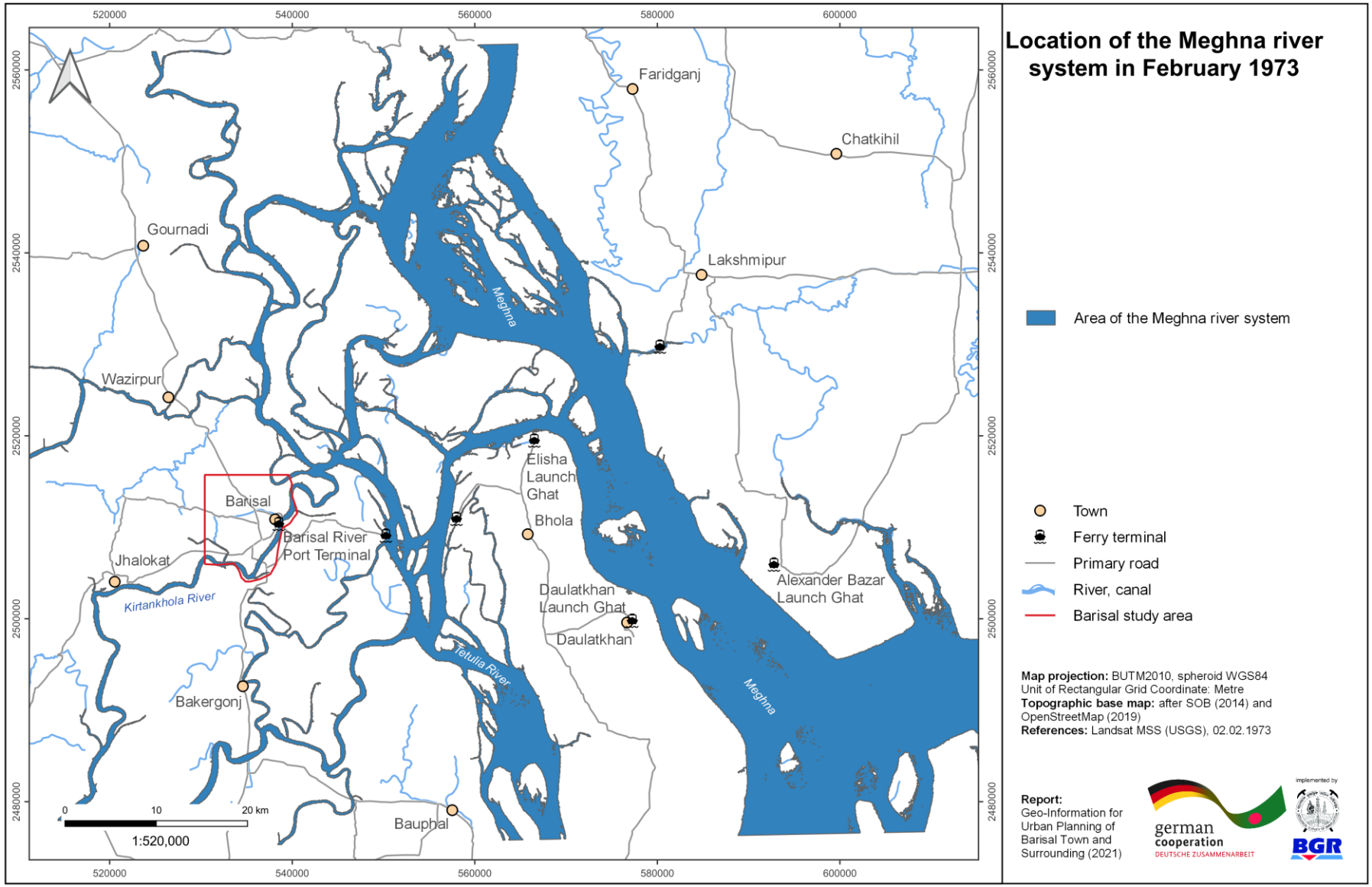

Figure A8: *Location of the Meghna river system based on NDWI from 1973.*

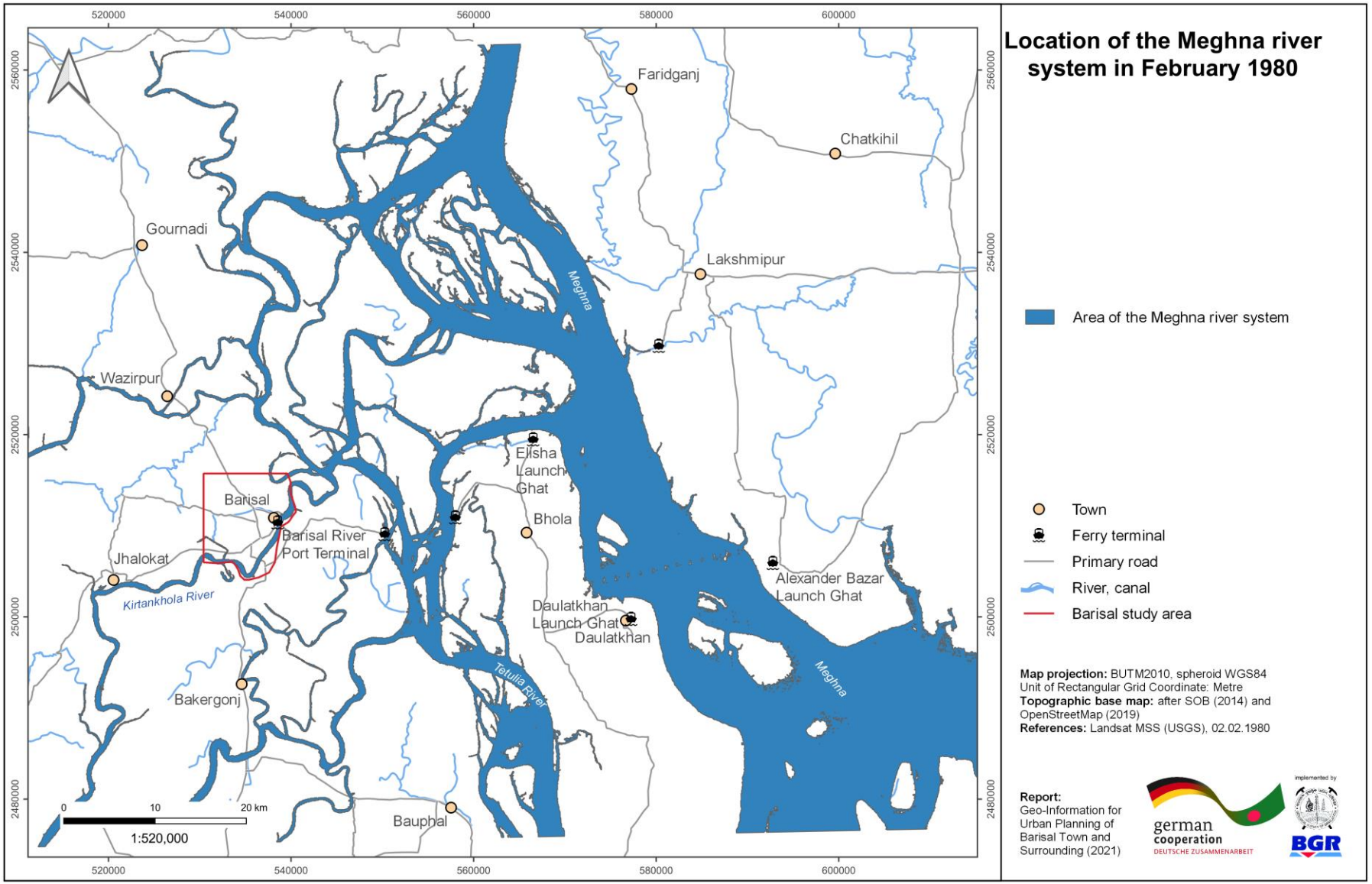

Figure A9: *Location of the Meghna river system based on NDWI from 1980.*

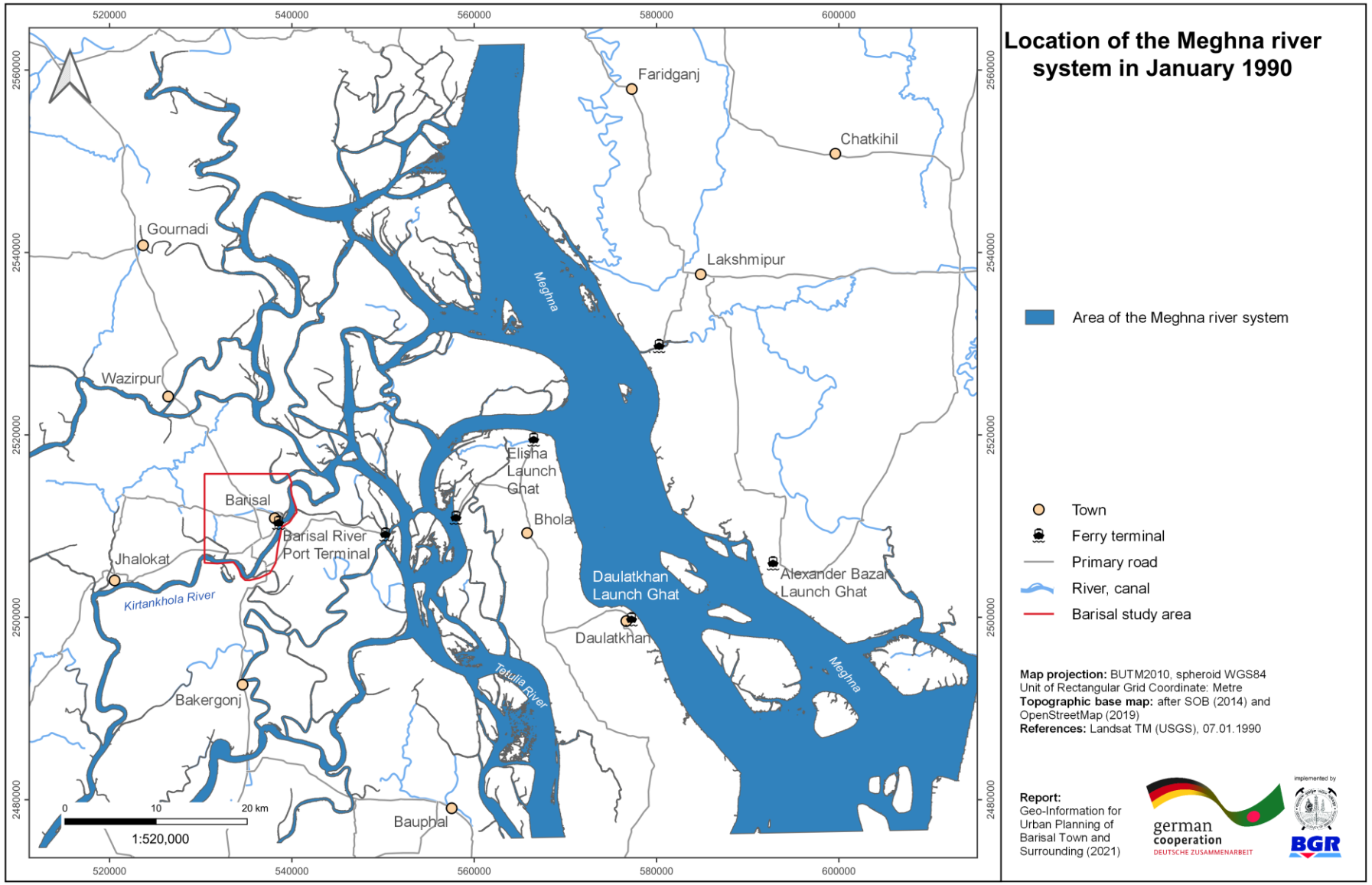

Figure A10: *Location of the Meghna river system based on NDWI from 1990.*

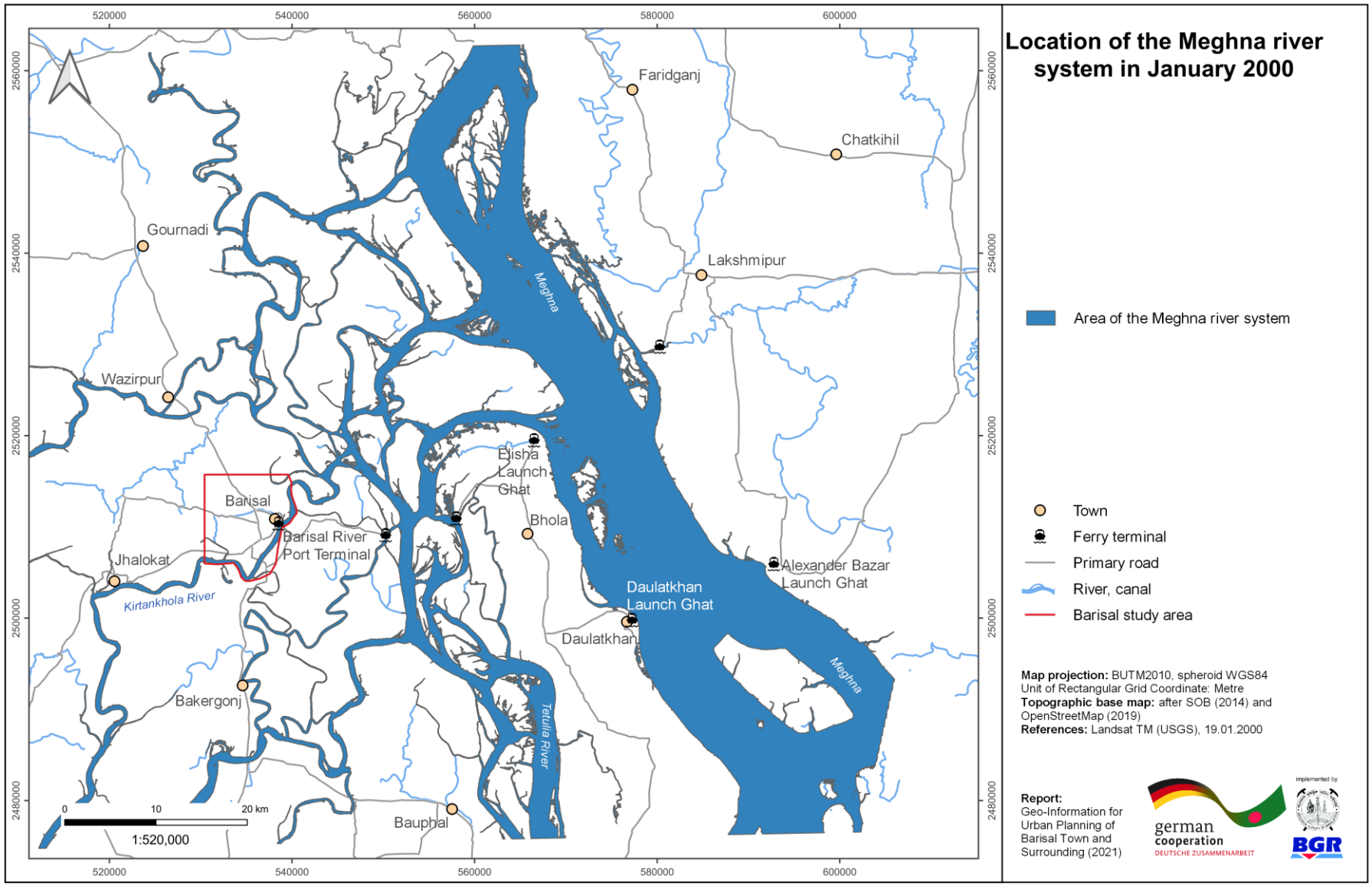

Figure A11: *Location of the Meghna river system based on NDWI from 2000.*

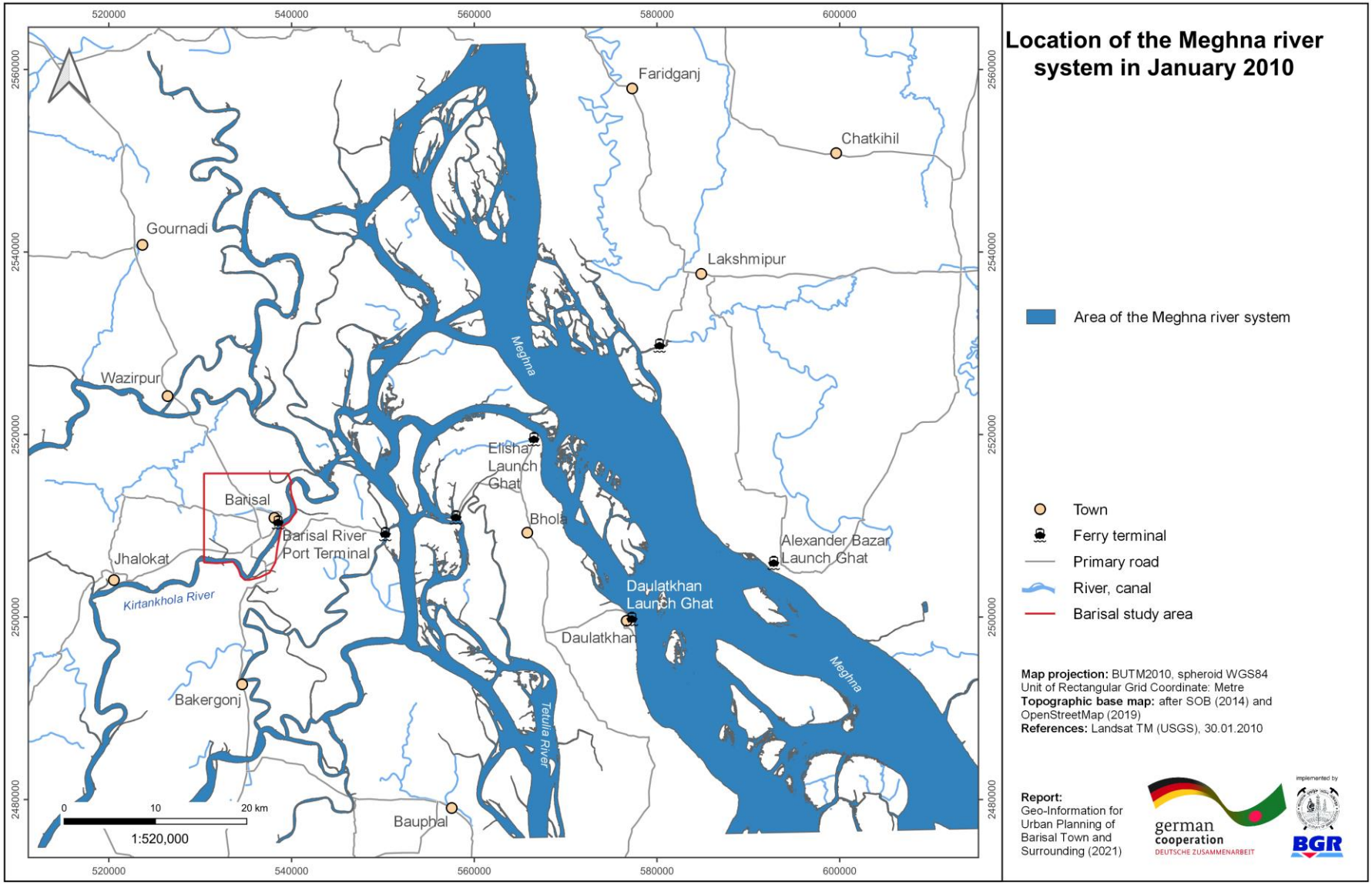

Figure A12: *Location of the Meghna river system based on NDWI from 2010.*

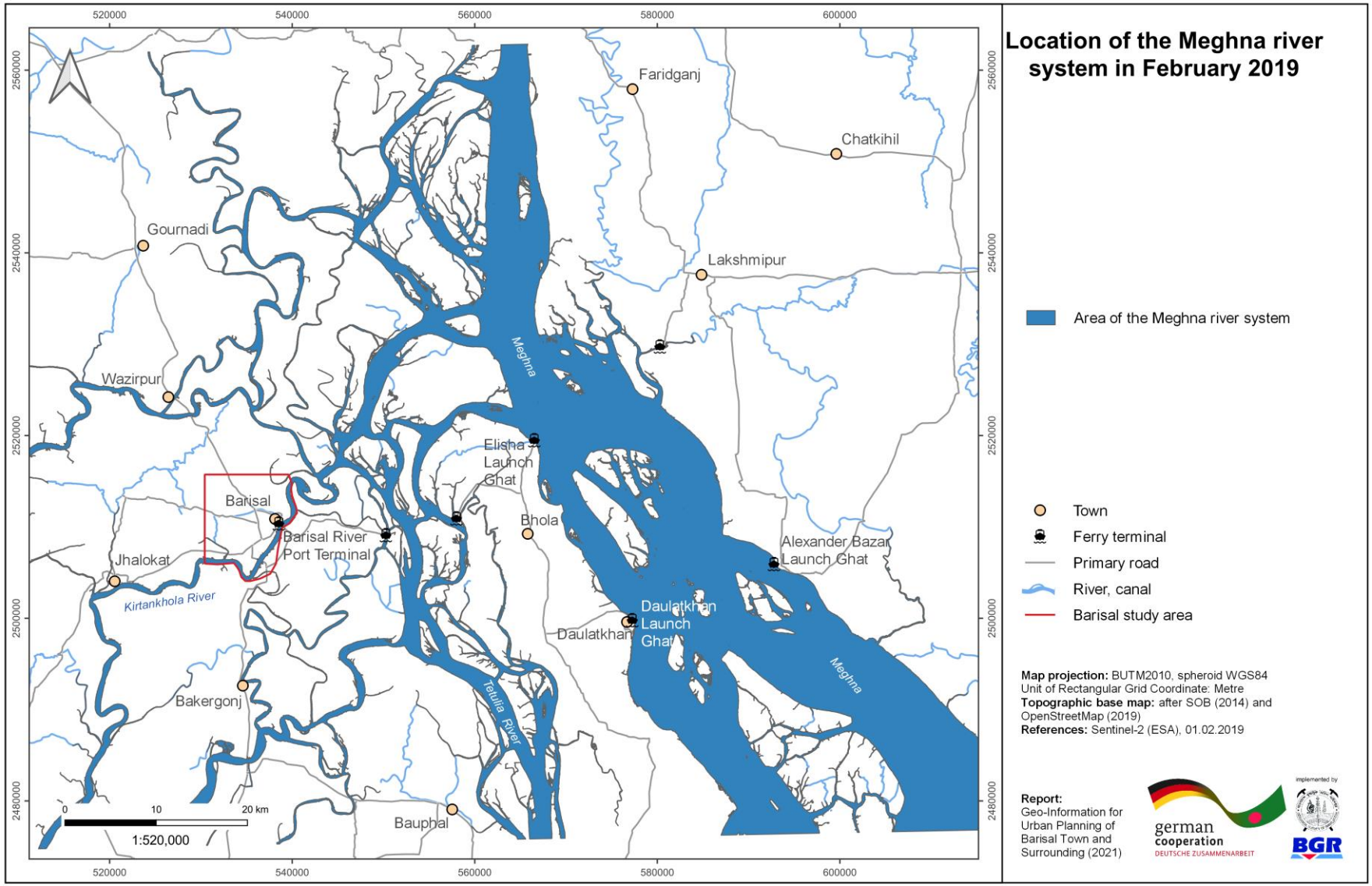

Figure A13: *Location of the Meghna river system based on NDWI from 2019.*

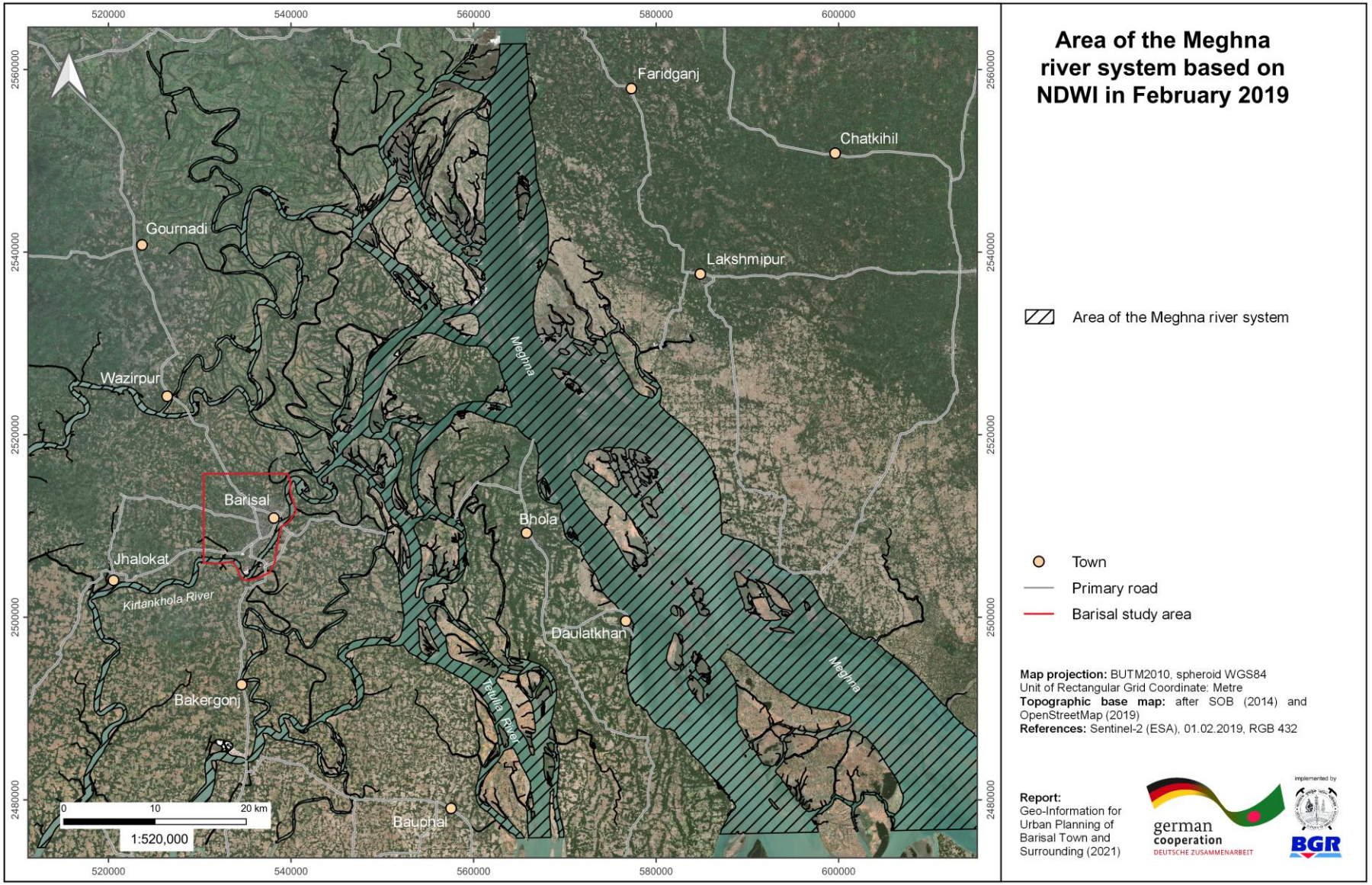

Figure A14: *Area of the Meghna river system based on NDWI from 2019.*

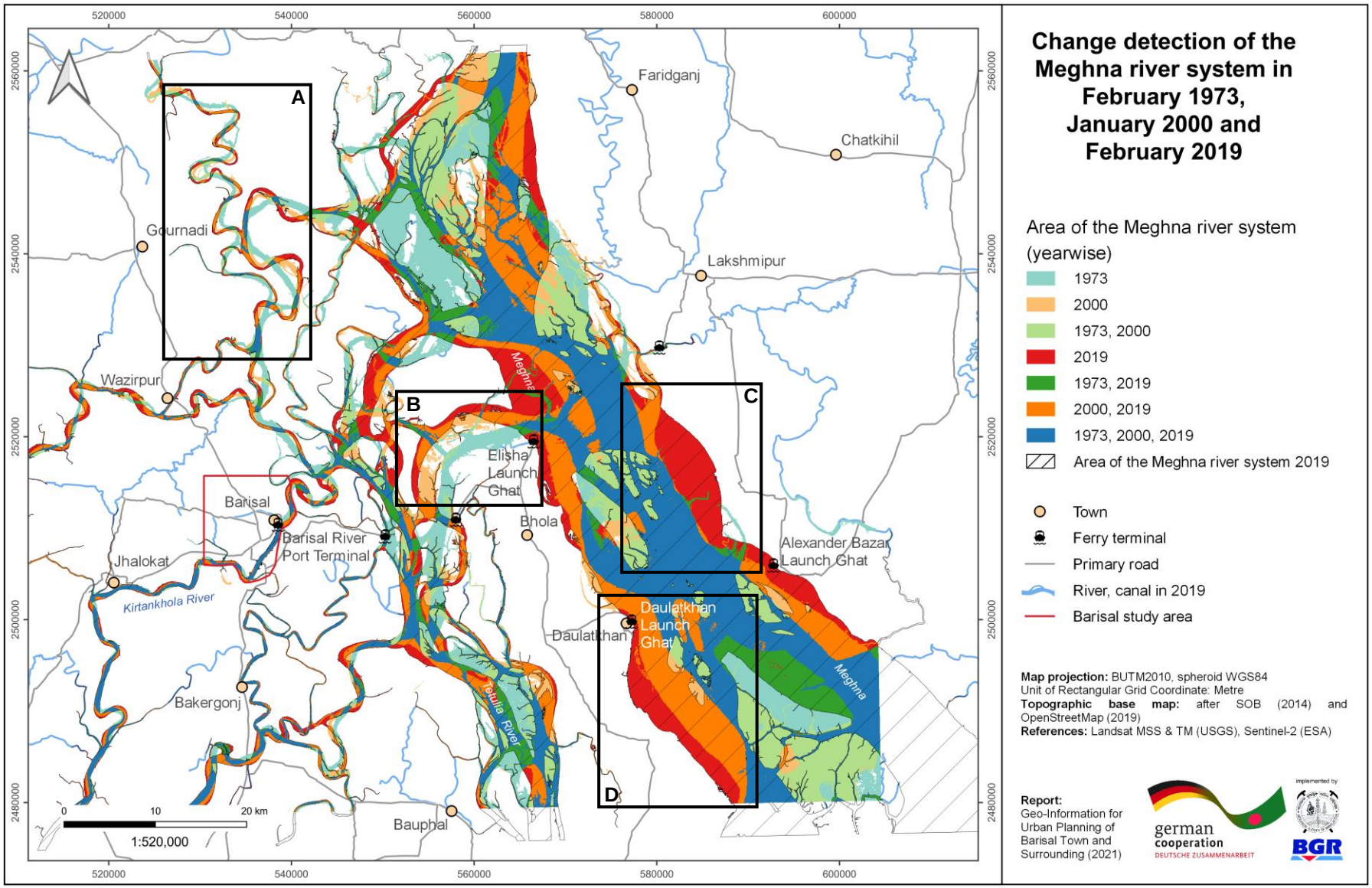

Figure A15: *Change detection of the Meghna river system of February 1973, January 2000 and February 2019.*

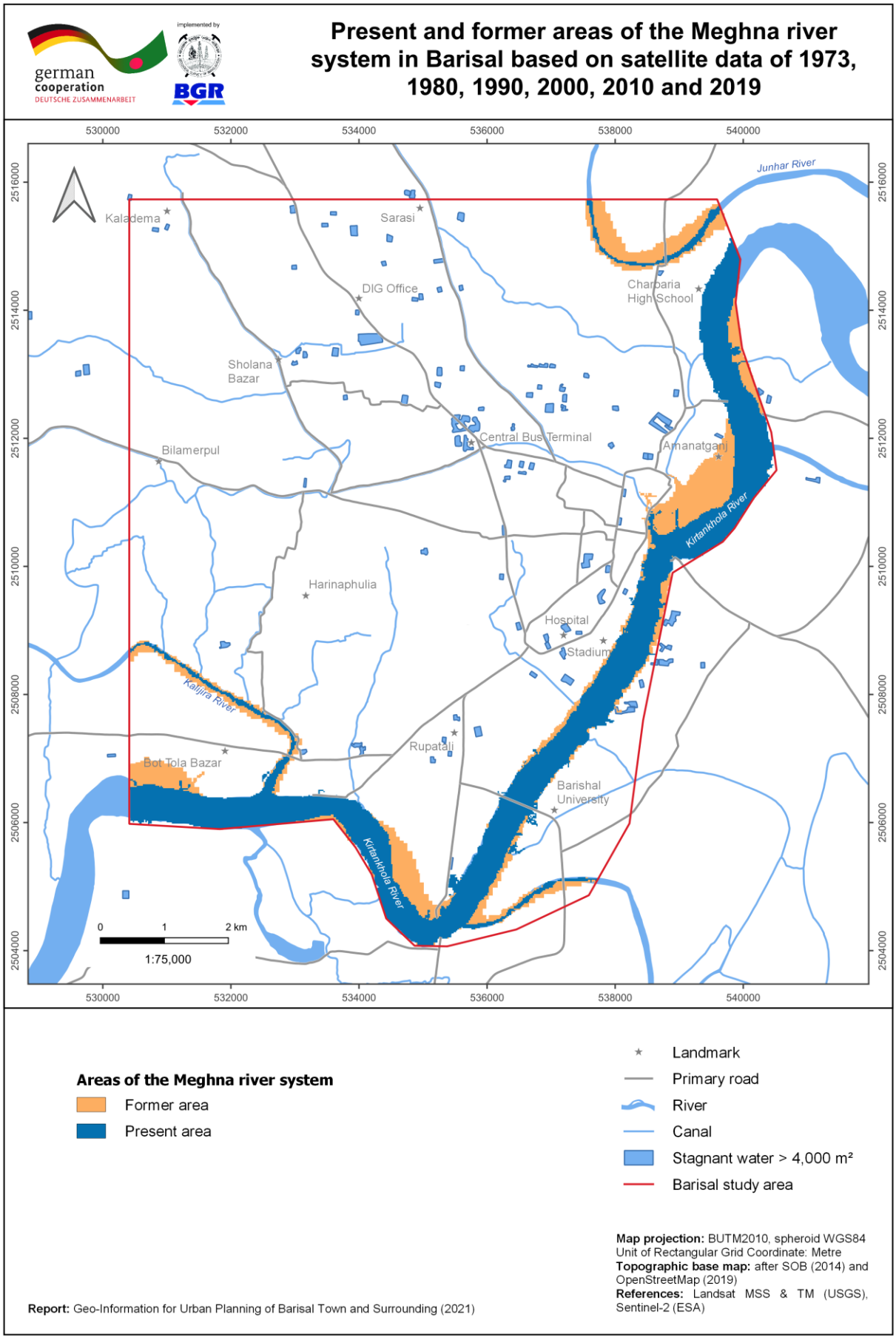

Figure A16: *Present and former areas of the Meghna river system in Barisal.*

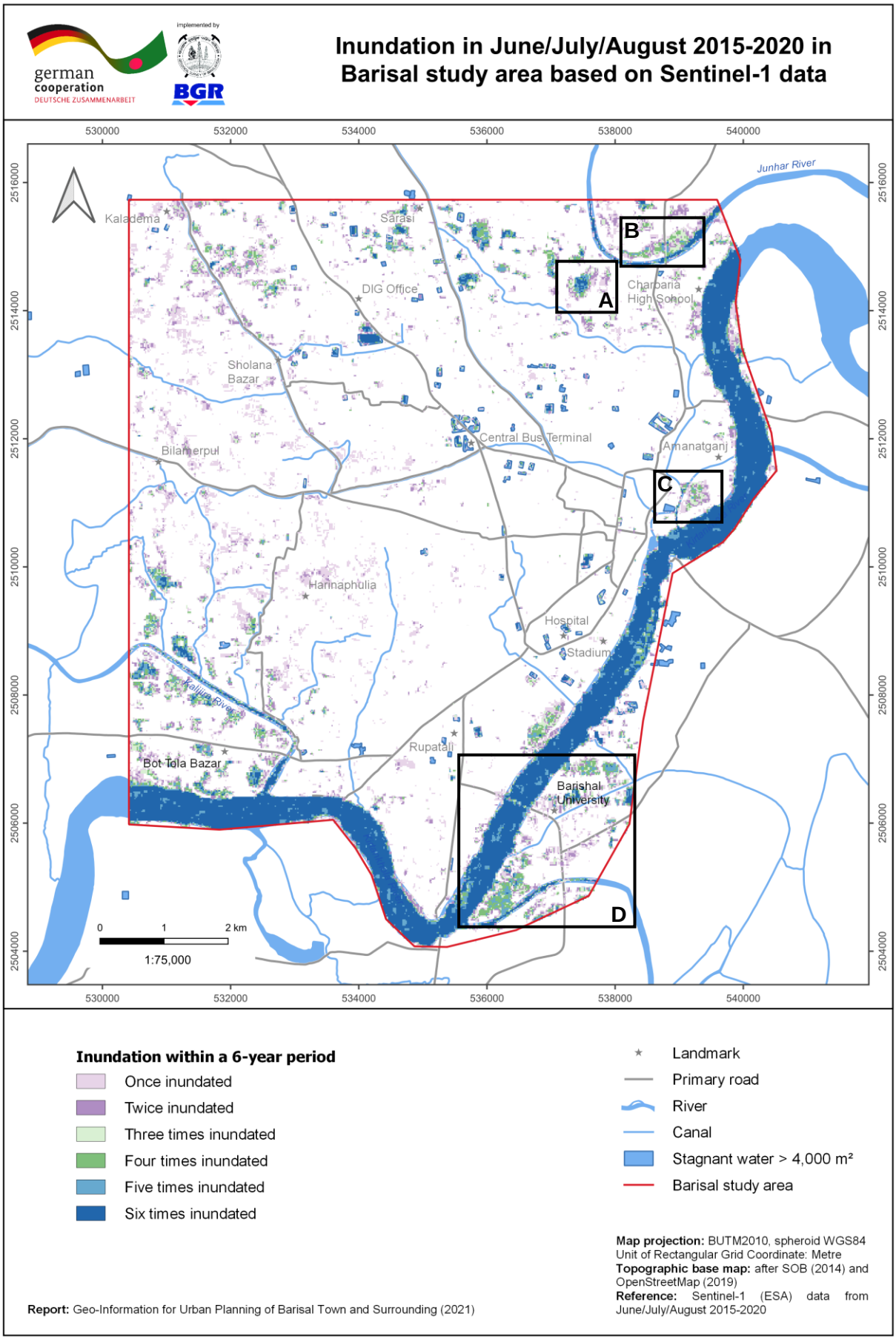

Figure A17: *Inundation in June/July 2015-2020 in Barisal study area.*

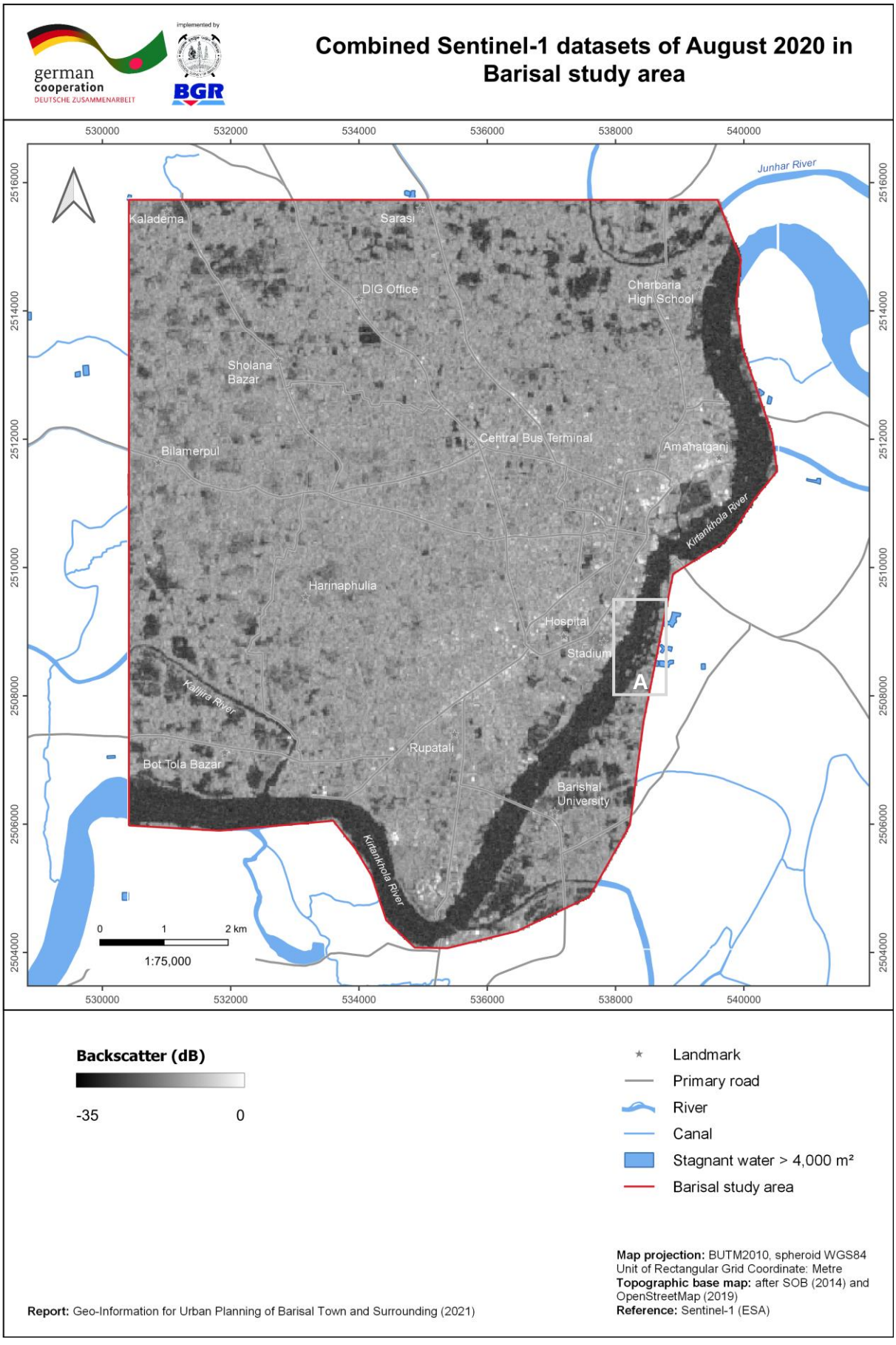

Figure A18: *Combined Sentinel-1 image of June/July 2020 in Barisal study area.*

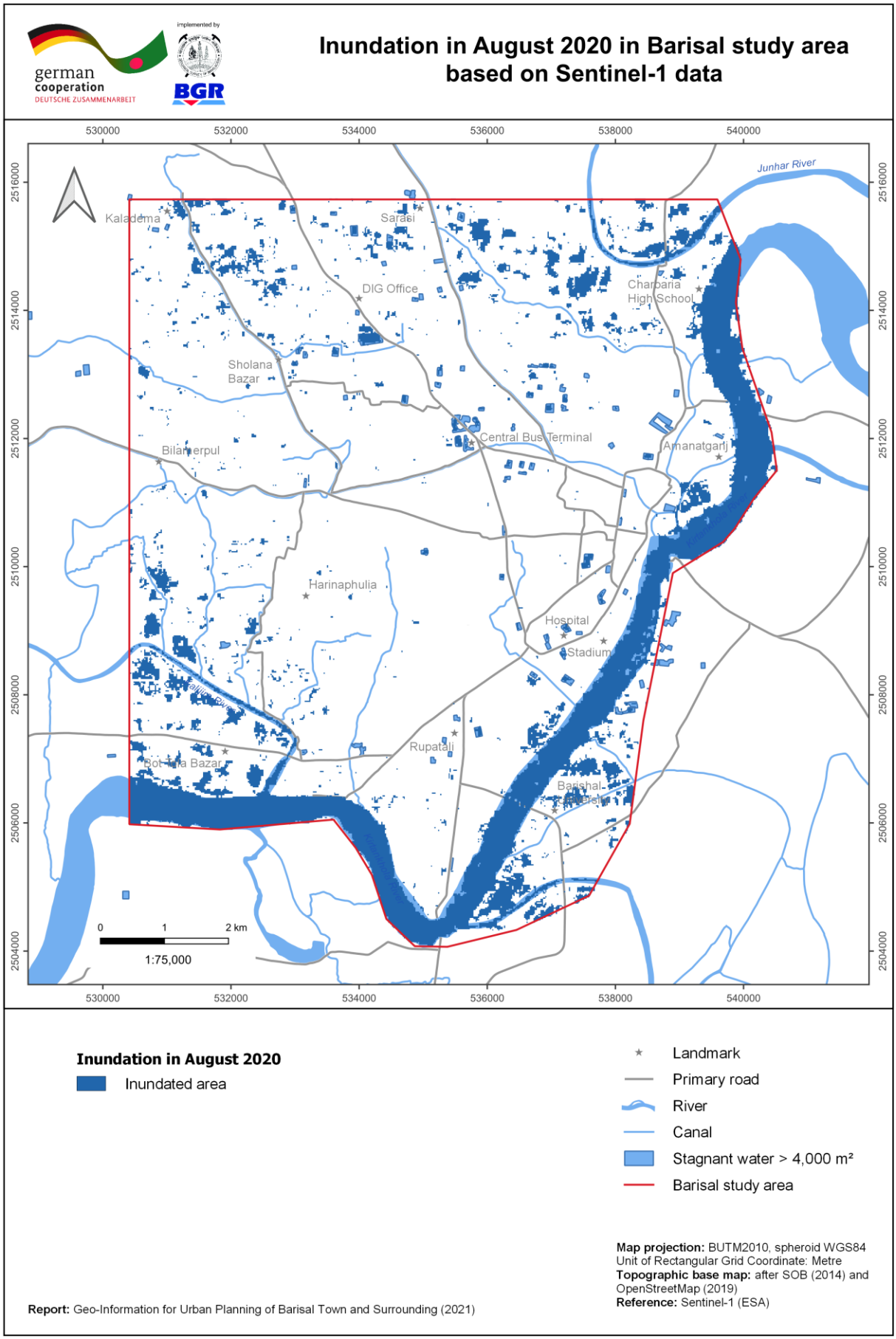

Figure A19: *Inundation in June/July 2020 in Barisal study area.*

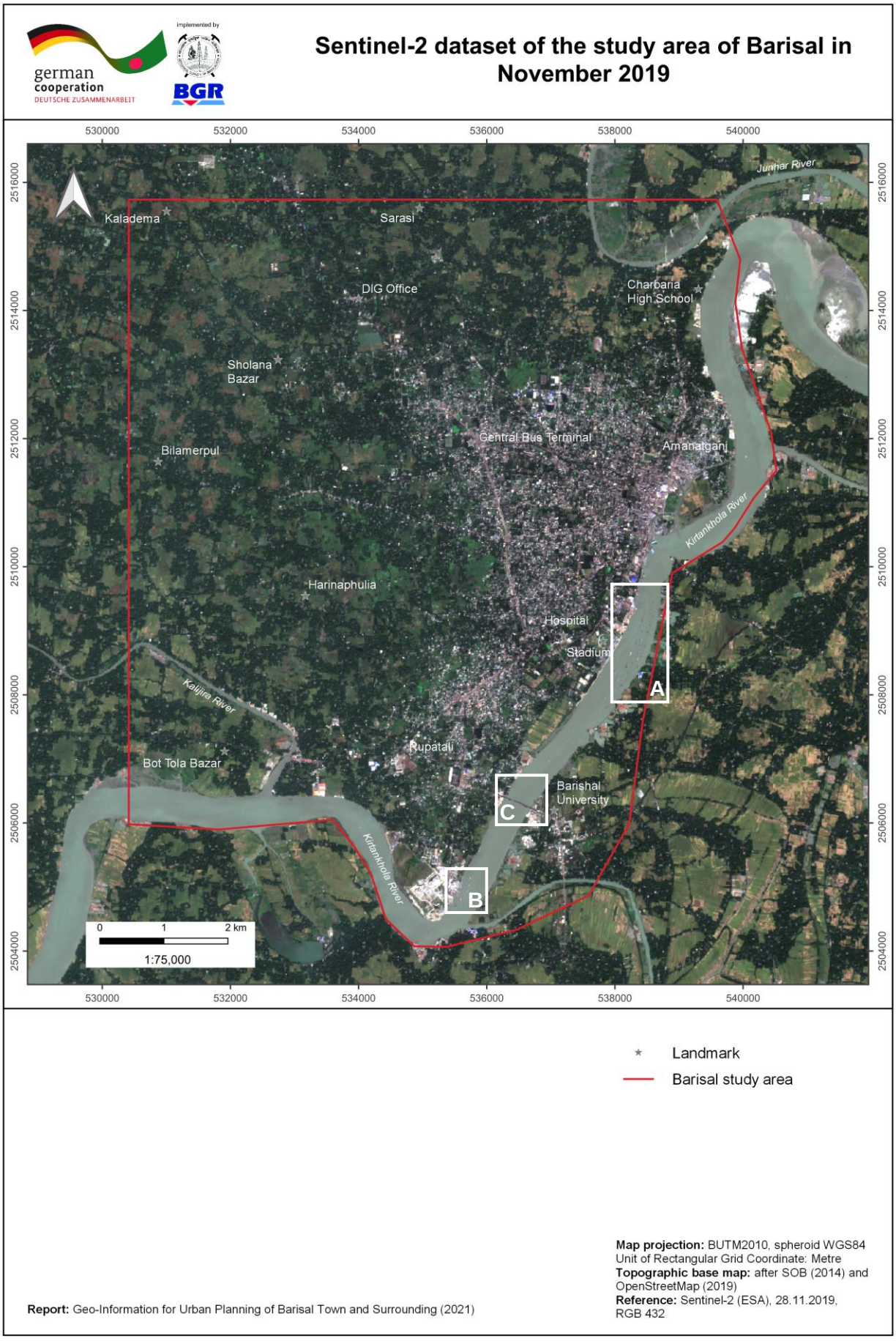

Figure A20: *Sentinel-2 dataset of the study area of Barisal.*

Annexure B: Google Earth Engine Code

```
// Select Area of Interest (pa = uploaded SHP of Barisal study area)
pa = pa.geometry();
// Center the map with focus on the study area
Map.centerObject(pa);


// 2015
// Define start and end date of the study period
var start_wet = '2015-07-01';
var end_wet = '2015-07-31';

// Load the Sentinel-1 image collection
var S1_wet15 = ee.ImageCollection('COPERNICUS/S1_GRD')
// Filter: Return only Vertical-Horizontal (VH) polarization images
.filter(ee.Filter.listContains('transmitterReceiverPolarisation', 'VH'))
// Filter: Return only images with the main acquisition mode IW
.filter(ee.Filter.eq('instrumentMode', 'IW'))
// Filter: Return only descending orbit images
.filter(ee.Filter.eq('orbitProperties_pass', 'DESCENDING'))
// Filter: Return only images with a 10 m resolution
.filterMetadata('resolution_meters','equals',10)
// Filter: Return only images within the study period
.filterDate(start_wet, end_wet)
// Filter: Return only images within the study area
.filterBounds(pa)
// Calculate the mean of all remaining images
.reduce(ee.Reducer.mean())
// Clip the mean-image to the study area
.clip(pa);
// Print the image information to the console
print(S1_wet15)


// 2016
var start_wet = '2016-06-01';
var end_wet = '2016-06-30';

var S1_wet16 = ee.ImageCollection('COPERNICUS/S1_GRD')
.filter(ee.Filter.listContains('transmitterReceiverPolarisation', 'VH'))
```

```
.filter(ee.Filter.eq('instrumentMode', 'IW'))
.filter(ee.Filter.eq('orbitProperties_pass', 'DESCENDING'))
.filterMetadata('resolution_meters','equals',10)
.filterDate(start_wet, end_wet)
.filterBounds(pa)
.reduce(ee.Reducer.mean())
.clip(pa);
print(S1_wet16)

// 2017
var start_wet = '2017-08-01';
var end_wet = '2017-08-31';

var S1_wet17 = ee.ImageCollection('COPERNICUS/S1_GRD')
.filter(ee.Filter.listContains('transmitterReceiverPolarisation', 'VH'))
.filter(ee.Filter.eq('instrumentMode', 'IW'))
.filter(ee.Filter.eq('orbitProperties_pass', 'DESCENDING'))
.filterMetadata('resolution_meters','equals',10)
.filterDate(start_wet, end_wet)
.filterBounds(pa)
.reduce(ee.Reducer.mean())
.clip(pa);
print(S1_wet17)

//2018
var start_wet = '2018-07-01';
var end_wet = '2018-07-31';

var S1_wet18 = ee.ImageCollection('COPERNICUS/S1_GRD')
.filter(ee.Filter.listContains('transmitterReceiverPolarisation', 'VH'))
.filter(ee.Filter.eq('instrumentMode', 'IW'))
.filter(ee.Filter.eq('orbitProperties_pass', 'DESCENDING'))
.filterMetadata('resolution_meters','equals',10)
.filterDate(start_wet, end_wet)
.filterBounds(pa)
.reduce(ee.Reducer.mean())
.clip(pa);
print(S1_wet18)

//2019
var start_wet = '2019-07-01';
var end_wet = '2019-08-31';
```

```
var S1_wet19 = ee.ImageCollection('COPERNICUS/S1_GRD')
.filter(ee.Filter.listContains('transmitterReceiverPolarisation', 'VH'))
.filter(ee.Filter.eq('instrumentMode', 'IW'))
.filter(ee.Filter.eq('orbitProperties_pass', 'DESCENDING'))
.filterMetadata('resolution_meters','equals',10)
.filterDate(start_wet, end_wet)
.filterBounds(pa)
.reduce(ee.Reducer.mean())
.clip(pa);
print(S1_wet19)

//2020
var start_wet = '2020-08-01';
var end_wet = '2020-08-31';

var S1_wet20 = ee.ImageCollection('COPERNICUS/S1_GRD')
.filter(ee.Filter.listContains('transmitterReceiverPolarisation', 'VH'))
.filter(ee.Filter.eq('instrumentMode', 'IW'))
.filter(ee.Filter.eq('orbitProperties_pass', 'DESCENDING'))
.filterMetadata('resolution_meters','equals',10)
.filterDate(start_wet, end_wet)
.filterBounds(pa)
.reduce(ee.Reducer.mean())
.clip(pa);
print(S1_wet20)

// Set threshold to distinguish between water and non-water
var threshold = -21

// Filter every image collection to the defined threshold
var S1_wet_threshold15 = S1_wet15.select('VH_mean').lt(threshold);
var S1_wet_threshold16 = S1_wet16.select('VH_mean').lt(threshold);
var S1_wet_threshold17 = S1_wet17.select('VH_mean').lt(threshold);
var S1_wet_threshold18 = S1_wet18.select('VH_mean').lt(threshold);
var S1_wet_threshold19 = S1_wet19.select('VH_mean').lt(threshold);
var S1_wet_threshold20 = S1_wet20.select('VH_mean').lt(threshold);

// Combining all images to get one image with six classes
var final_img =
S1_wet_threshold15.add(S1_wet_threshold16).add(S1_wet_threshold17).add(S1_w
et_threshold18).add(S1_wet_threshold19).add(S1_wet_threshold20);
// Visualize the final result
```

```
Map.addLayer(final.updateMask(final_img),{palette:"0000FF"},'Water
extent',1);

// Export the image to the Drive
Export.image.toDrive({
// Definition of the image
  image: final_img,
// Description
  description: 'Barisal_Inun_Map',
// Resolution in meter
  scale: 20,
// Study area
  region: pa,
// Format of the raster
  fileFormat: 'GeoTIFF'
});

Export.image.toDrive({
  image: S1_wet20.select("VH_mean"),
  description: 'Barisal_2020_image',
  scale: 10,
  region: pa,
  fileFormat: 'GeoTIFF'
});

Export.image.toDrive({
  image: S1_wet_threshold20,
  description: 'Barisal_2020_inundation',
  scale: 10,
  region: pa,
  fileFormat: 'GeoTIFF'
});
```

Annexure C: Data

Optical satellite images

Landsat naming convention

Image name: LXSS_LLLL_PPPRRR_YYYYMMDD_yyyymmdd_CC_TX

Group	**Meaning**		
LXSS	L: Landsat	X: Sensor “M” (MSS), “T” (TM)	SS: Satellite “01” (Landsat 1), “03” (Landsat 3), “05” (Landsat 5)
LLLL	Processing correction level: “L1TP”, “L1GT”, “L1GS”, “L2SP”		
PPPRRR	PPP: WRS path		RRR: WRS row
YYYYMMDD	Acquisition year, month, day		
yyyymmdd	Processing year, month, day		
CC	Collection number: “01”, “02”, …		
TX	Collection category: “RT” (Real-Time), “T1” (Tier 1), “T2” (Tier 2)		

Source: usgs.gov/faqs/how-can-i-tell-difference-between-landsat-collections-data-and-landsat-data-i-have-downloaded (Accessed on 20-07-2020).

Data (Landsat MSS, Level-1)

Year	Image name	Product
1973	LM01_L1TP_147044_19730202_20200909_02_T2	River Shifting Change Detection Analysis
1980	LM03_L1TP_147044_19800202_20200905_02_T2	River Shifting Change Detection Analysis

Data (Landsat TM, Level-2)

Year	Image name	Product
1990	LT05_L2SP_137044_19900107_20200916_02_T1	River Shifting Change Detection Analysis
2000	LT05_L2SP_137044_20000119_20200907_02_T1	River Shifting Change Detection Analysis
2010	LT05_L2SP_137044_20100130_20200825_02_T1	River Shifting Change Detection Analysis

Sentinel-2 naming convention

Image name: MMM_MSIXXX_YYYYMMDDHHMMSS_Nxxyy_ROOO_Txxxxx_<Product Discriminator>

Group	Meaning
MMM	Mission ID: “S2A”, “S2B”
MSIXXX	Product level: “Level-1C”, “Level-2A”
YYYYMMDDTHHMMSS	Sensing start time, date and time separated by character “T”
Nxxyy	PDGS processing baseline number
ROOO	Relative orbit number
Txxxxx	Tile number

Source: sentinel.esa.int/web/sentinel/user-guides/sentinel-2-msi/naming-convention (Accessed on 20-07-2020).

Data

Year	Image name	Product
2019	S2A_MSIL2A_20190201T043011_N0211_R133_T46QBK_20190201T082036	River Shifting Change Detection Analysis
	S2A_MSIL2A_20190201T043011_N0211_R133_T46QBL_20190201T082036	River Shifting Change Detection Analysis
	S2A_MSIL2A_20191128T043131_N0213_R133_T46QBL_20191128T083132	Land-Use Classification

RADAR satellite images

Sentinel-1 naming convention

Image name: MMM_BB_TTTR_LFPP_YYYYMMDDTHHMMSS_ YYYYMMDDTHHMMSS_OOOOOO_DDDDDD_CCCC

Group	Meaning		
MMM	Mission Identifier: “S1A”, S1B”		
BB	Mode/Beam: “S1/S2/S3/S4/S5/S6”, “IW/EW/WV”		
TTTR	TTT: Product Type “RAW”, “SLC”, “GRD”, “OCN”	R: Resolution Class “F” (Full), “H” (High), “M” (Medium)	
LFPP	L: Processing Level “0”, “1”, “2”	F: Product Class “S” (Standard), “A” (Annotation)	PP: Polarization “SH” (single HH) “SV” (single VV) “DH” (dual HH+HV) “DV” (dual VV+VH)
YYYYMMDDTHHMMSS	Product start time, separated by the character “T”		

YYYYMMDDTHHMMSS	Product end time, separated by the character “T”
OOOOOO	Absolute orbit number at product start time
DDDDDD	Mission data-take identifier
CCCC	Product unique identifier

Source: sentinel.esa.int/web/sentinel/user-guides/sentinel-1-sar/naming-conventions (Accessed on 20-07-2020).

Data: Inundation Mapping

Year	Image Name
2015	S1A_IW_GRDH_1SDV_20150706T235549_20150706T235614_006697_008F55_901C
2016	S1A_IW_GRDH_1SDV_20160606T235552_20160606T235617_011597_011B95_8496
2017	S1A_IW_GRDH_1SDV_20170824T235558_20170824T235623_018072_01E586_FF38
	S1A_IW_GRDH_1SDV_20170812T235557_20170812T235622_017897_01E03B_D81A
2018	S1A_IW_GRDH_1SDV_20180714T235602_20180714T235627_022797_0278AA_BFC4
	S1A_IW_GRDH_1SDV_20180726T235603_20180726T235628_022972_027E33_0CE9
2019	S1A_IW_GRDH_1SDV_20190709T235608_20190709T235633_028047_032AE1_EBE3
	S1A_IW_GRDH_1SDV_20190721T235609_20190721T235634_028222_033027_D84D
	S1A_IW_GRDH_1SDV_20190802T235609_20190802T235634_028397_03357D_AEEC
	S1A_IW_GRDH_1SDV_20190826T235611_20190826T235636_028747_03414E_B972
2020	S1A_IW_GRDH_1SDV_20200808T235616_20200808T235641_033822_03EBE2_0A06
	S1A_IW_GRDH_1SDV_20200820T235617_20200820T235642_033997_03F204_62E3